

國立交通大學

電機資訊學院 電子與光電學程

碩士論文

氧化侷限面射型雷射之二維(時間和空間)模擬分析

The spatiotemporal modeling of oxide-confined  
Vertical-Cavity Surface-Emitting Lasers



研究生：羅俊麟

指導教授：郭浩中

中華民國九十三年六月

# 氧化侷限面射型雷射之二維(時間和空間)模擬分析

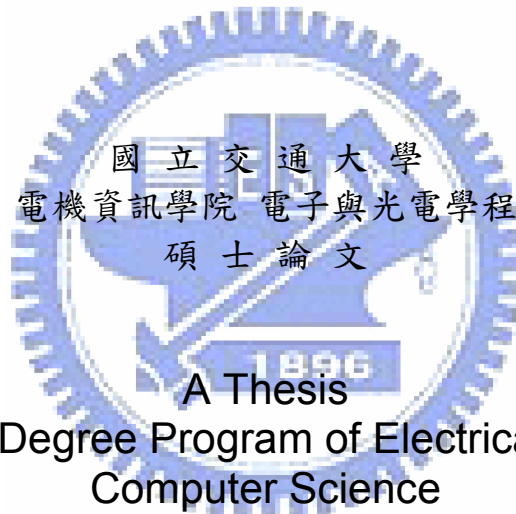
The spatiotemporal modeling of oxide-confined  
Vertical-Cavity Surface-Emitting Lasers

研究 生：羅俊麟

Student : Chun-Lin Lo

指導教授：郭浩中

Advisor : Dr. Hao-Chung Kuo



Submitted to Degree Program of Electrical Engineering  
Computer Science

College of Electrical Engineering and Computer Science

National Chiao Tung University

in Partial Fulfillment of the Requirements

for the Degree of

Master of Science

in

Electronics and Electro-Optical Engineering

June 2004

Hsinchu, Taiwan, Republic of China

中華民國九十三年六月

# 國立交通大學

## 論文口試委員會審定書

本校 電機資訊學院專班 電子與光電 組 羅俊麟 君

所提論文

(中文) 氧化侷限面射型雷射之二維(時間和空間)模擬分析

(英文) The spatiotemporal modeling of oxide-confined  
Vertical-Cavity Surface-Emitting Lasers

合於碩士資格水準、業經本委員會評審認可。

口試委員：

宋嘉斌 林恭如

宋 嘉 斌

林 恭 如

陳智弘 2004-6-16.

陳 智 弘

指導教授：

郭 浩 中

郭 浩 中

班主任：

郭 仁 財

郭 仁 財

中華民國 93 年 6 月 16 日

# 國立交通大學

## 博碩士論文著作權授權書

(提供授權人裝訂於紙本論文中書名頁之次頁用)

本授權書所授權之論文為本人在國立交通大學(學院)電機資訊學院碩士在職專班 電子系流電組，92學年度第 三 學期取得碩士學位之論文。

論文名稱：氧化偶限面射型雷射之二維(時間和空間)模擬分析  
指導教授：郭浩中

同意  不同意 (國科會科學技術資料中心重製上網)

本人具有著作財產權之上列論文全文(含摘要)資料，授予行政院國家科學委員會科學技術資料中心(或改制後之機構)，得不限地域、時間與次數以微縮、光碟或數位化等各種方式重製後散布發行或上載網路。  
本論文為本人向經濟部智慧財產局申請專利(未申請者本條款請不予理會)的附件之一，申請文號為：\_\_\_\_\_，註明文號者請將全文資料延後半年再公開。

同意  不同意 (圖書館紙本影印)

本人具有著作財產權之上列論文全文(含摘要)資料，授予教育部指定送繳之圖書館及國立交通大學圖書館，基於推動讀者間「資源共享、互惠合作」之理念，與回饋社會及學術研究之目的，教育部指定送繳之圖書館及國立交通大學圖書館得以紙本收錄、重製與利用；於著作權法合理使用範圍內，不限地域與時間，讀者得進行閱覽或列印。  
本論文為本人向經濟部智慧財產局申請專利(未申請者本條款請不予理會)的附件之一，申請文號為：\_\_\_\_\_，註明文號者請將全文資料延後半年再公開。

同意

本人具有著作財產權之上列論文全文(含摘要)，授予國立交通大學與台灣聯合大學系統圖書館，基於推動讀者間「資源共享、互惠合作」之理念，與回饋社會及學術研究之目的，國立交通大學圖書館及台灣聯合大學系統圖書館得不限地域、時間與次數，以微縮、光碟或其他各種數位化方式將上列論文重製，並得將數位化之上列論文及論文電子檔以上載網路方式，於著作權法合理使用範圍內，讀者得進行線上檢索、閱覽、下載或列印。

論文全文上載網路公開之範圍及時間：

本校及台灣聯合大學系統區域網路	<input type="checkbox"/> 立即公開
校外網際網路	<input type="checkbox"/> 立即公開

上述授權內容均無須訂立讓與及授權契約書。依本授權之發行權為非專屬性發行權利。依本授權所為之收錄、重製、發行及學術研發利用均為無償。上述同意與不同意之欄位若未勾選，本人同意視同授權。

研究生：羅俊麟

學號：9167508

親筆正楷：羅俊麟 (務必填寫)

中華民國 93 年 6 月 21 日

## 國家圖書館 博碩士論文電子檔案上網授權書

(提供授權人裝訂於紙本論文中博碩士論文授權書之次頁用)

本授權書所授權之論文為本人在國立交通大學(學院)電機資訊學院  
碩士在職專班 電子與光電組，92 學年度第 二 學期取得碩士學  
位之論文。

論文名稱：氧化偏限面射型雷射之二維(時間和空間)模擬分析  
指導教授：郭浩中

### ■ 同意

本人具有著作財產權之上列論文全文(含摘要)，以非專屬、無償授  
權國家圖書館，不限地域、時間與次數，以微縮、光碟或其他各種  
數位化方式將上列論文重製，並得將數位化之上列論文及論文電子  
檔以上載網路方式，提供讀者基於個人非營利性質之線上檢索、閱  
覽、下載或列印。

上述授權內容均無須訂立讓與及授權契約書。依本授權之發行權為  
非專屬性發行權利。依本授權所為之收錄、重製、發行及學術研發  
利用均為無償。上述同意與不同意之欄位若未勾選，本人同意視同  
授權。

研究生：羅俊麟

學號：9167508

親筆正楷：羅俊麟 (務必填寫)

中華民國 93 年 6 月 21 日

本授權書請以黑筆撰寫，並列印二份，其中一份影印裝訂於附錄三之一(博碩士論文授權  
書)之次頁；另一份於辦理離校時繳交給系所助理，由圖書館彙總寄交國家圖書館。

# 氧化侷限面射型雷射之二維(時間和空間)模擬分析

學生：羅俊麟

指導教授：郭浩中 博士

國立交通大學電機資訊學院 電子與光電學程（研究所）碩士班

## 摘要

本篇論文主要是以元件模擬分析的技術來探討弱折射率波導面射型雷射 (weakly index-guided VCSELs) 的特性。而根據氧化侷限面射型雷射 (oxide-confined VCSELs) 的物理特性和材料結構，我們可以建立一個三維的元件模型(其中有二維為空間向量，一維為時間向量)。藉由對載子密度速率方程式 (carrier rate equation) 和光子密度速率方程式 (photon rate equation) 的數值分析運算，並考量其熱效應、漏電流效應 (leakage current effect) 、電流散佈效應 (current spreading effect) 和載子擴散效應 (carrier diffusion effect) 而模擬出輸出功率的多模暫態響應、光-電流的特性曲線、光模態的競爭 (mode competition) 、空間燒洞 (spatial hole burning) 和小信號調變。

我們也發現當不考慮載子傳輸效應 (carrier transport effect) 時，電流散佈效應會比載子擴散在動態響應方面有較顯著的影響。在較低的電流散佈條件下，其可以得到較高的頻寬和較佳的低頻響應；推論其原因為較低的電流散佈將增加主動層中心區域 (core region) 的電流密度，因而具備較低的臨界電流 (threshold current) ，而呈現較佳的頻率響應特性。

面射型雷射的設計和製造是一項昂貴、耗時且需繁複製程步驟的工作。藉由本篇論文對模擬分析的研究，恰可提供一個準確又有效率的元件模型，進而縮短元件的設計週期並加速元件製程的發展。

# The spatiotemporal modeling of oxide-confined Vertical-Cavity Surface-Emitting Lasers

Student : Chun\_Lin Lo

Advisor : Dr. Hao\_Chung Kuo

Degree Program of Electrical Engineering Computer Science  
National Chiao Tung University

## ABSTRACT

The spatiotemporal simulation for weakly index-guided vertical-cavity surface-emitting lasers (VCSELs) are presented in this work. A three dimensional model (2 dimension in space domain and 1 dimension in time domain) is proposed based on physical and geometrical properties of oxide confined VCSELs. By solving carrier and photon rate equations numerically with thermal effect, current leakage effect, current spreading effect and carrier diffusion effect, we demonstrated the simulation capability including the multimode transient response of output power, light-current (LI) characteristics, optical mode competition, spatial hole burning (SHB), and small-signal modulation of VCSELs.

The influence of spreading current was found to be more dominative over carrier diffusion on dynamic response while the carrier transport is neglected. A higher bandwidth and better low frequency response are obtained under low current spreading condition that increases the current concentrated in the core region of the active layer results in low threshold current.

Design and fabrication of VCSELs, is expensive, time-consuming, and needs iterative process. This simulation tool provides an accurate and efficient device modeling, and can help on shortening the design cycle, and speed up the development process.

# ACKNOWLEDGEMENTS

This work was supported by the Semiconductor Laser Technology Laboratory of Institute of Electro-optical Engineering in National Chiao-Tung University (NCTU), Taiwan. The author would like to thank his teacher and colleagues who have made great contributions to this work. They include Pro.Hao\_chung Kuo (郭浩中 老師), Ya\_Hsien Chang (張亞銜 學長) who is a candidate for doctor's degree, Chun\_Yi Lu (呂俊毅 同學) and Gwo\_Feng Tzeng (曾國峰 學弟) at the laboratory. Specially thanks to Ya\_Hsien Chang's help and guidance during this research.

Finally, the author would like to present his the most highly appreciation to Prof.Kuo who providing the opportunity for author to join his research group.

Chun\_Lin Lo (羅俊麟)

*Hsin Chu City (新竹)*  
*June 2004*

# CONTENTS

中文摘要 -----	I
ABSTRACT -----	II
ACKNOWLEDGEMENTS -----	III
CONTENTS -----	IV
FIGURES -----	V
TABLES -----	VII
CHAPTER 1 Introduction -----	1
CHAPTER 2 Rate equations -----	8
2.1 Carrier Rate Equation -----	8
2.1.1 Pumping Energy -----	9
2.1.2 Stimulated absorption and stimulated emission -----	10
2.1.3 Spontaneous recombination -----	14
2.1.4 Non-radiative recombination -----	15
2.2 Photon Rate Equation -----	17
CHAPTER 3 Models and parameters -----	22
3.1 Device Structure and materials -----	22
3.2 Rate Equations -----	25
3.3 Thermal Model -----	26
3.4 LP modes calculation -----	29
3.5 Flow Chart of Algorithm -----	40
CHAPTER 4 Simulation results and numerical analysis -----	41
4.1 The transient response of output power -----	41
4.2 L-I curve -----	48
4.3 Spatial Hole Burning -----	50
4.4 Thermal effect -----	54
4.5 Small Signal Modulation -----	55
CHAPTER 5 Conclusions -----	58
REFERENCES -----	60
作者簡介 -----	62

## FIGURES

<b>Figure 1.1</b>	Millions of VCSELs on a single wafer	1
<b>Figure 1.2</b>	VCSEL structure	2
<b>Figure 1.3</b>	Carrier distribution in the active region	4
<b>Figure 1.4</b>	Transverse field distribution of LP01 and LP11	5
<b>Figure 1.5</b>	The working environment of MATLAB	5
<b>Figure 2.1</b>	The individual terms considered by general carrier rate equation	9
<b>Figure 2.2</b>	The continuous pumping is the essential condition to reach population inversion	10
<b>Figure 2.3</b>	Stimulated absorption generates more electron-hole pairs. Stimulated emission produced coherent light (same energy, phase, propagation direction, highly monochromatic)	11
<b>Figure 2.4</b>	The interaction of stimulated absorption and stimulated emission contribute the optical gain of material. The “gain” represents in this figure is just the ratio of photons that is not the same as “material gain” we will discuss later. It also presents the gain is the function of photons traveling length	12
<b>Figure 2.5</b>	The material gain $G$ and differential gain $g_0$ are the function of $N$	13
<b>Figure 2.6</b>	Spontaneous recombination emits incoherent light in all directions which is a random process	14
<b>Figure 2.7</b>	Comparing spectra for spontaneous and stimulated emission	15
<b>Figure 2.8</b>	Two non-radiative recombination mechanisms	16
<b>Figure 2.9</b>	The individual terms considered by general photon rate equation	18
<b>Figure 2.10</b>	DBR	19
<b>Figure 3.1</b>	Schematic of a cylindrical weakly index-guided structure	23
<b>Figure 3.2</b>	The conceptual scheme of thermal model	27
<b>Figure 3.3</b>	Temperature effects on gain and cavity resonance ( Red: gain spectrum, Green: cavity resonance)	28
<b>Figure 3.4</b>	The ordinary Bessel function of the first kind $J_l$ and order $l=0,1,2,3$ .	33
<b>Figure 3.5</b>	The modified Bessel function of the second kind $K_l$ and order $l=0,1,2,3$ .	33
<b>Figure 3.6</b>	The graphical solution of $m^{th}$ of $l=0$ .	35
<b>Figure 3.7</b>	$l=0,1,2,3,4$ , $V=6.9906$ and their associated $X$ roots and $m^{th}$ .	36
<b>Figure 3.8</b>	The 1-D intensity radial distribution of various LP modes. Assuming $A'=1$ , $\cos(l\phi)$ and $\sin(l\phi)$ factors are not taken into account.	36
<b>Figure 3.9</b>	The field distribution of four lower LP modes with $\cos(l\phi)$ term.	37

<b>Figure 3.10</b>	The field distribution of four lower LP modes with $\sin(l\phi)$ term. It is obviously there is no $\sin$ contribution for $LP_{0m}$ modes. -----	37
<b>Figure 3.11</b>	The field distribution of four lower LP modes with $\cos(l\phi)$ and $\sin(l\phi)$ term. -----	38
<b>Figure 3.12</b>	Variation of the normalized propagation constant $b$ with normalized frequency $V$ for a step index fiber corresponding to various LP modes. -----	39
<b>Figure 3.13</b>	The most important interrelationship between individual physical process. -----	40
<b>Figure 4.1</b>	The transient response of VCSELs with 6mA, 3mA and 1mA, respectively. $Rox=2\mu m$ . -----	42
<b>Figure 4.2</b>	The single mode operation. The LP01 mode is called fundamental mode. -----	43
<b>Figure 4.3</b>	The multimode behavior of VCSELs. The output optical profile are also shown. (dash line: total power) -----	43
<b>Figure 4.4</b>	Without current confinement ( $sp=1\mu m$ ), for (a) The transient response of two transverse modes. (b) The corresponding of time evolution of carrier distribution. $Rox=1\mu m$ , $I=2mA$ , $DN=15cm^2/s$ . -----	45
<b>Figure 4.5</b>	With current confinement ( $sp=0\mu m$ ), for (a) The transient response of two transverse modes. (b) The corresponding of time evolution of carrier distribution. $Rox=1\mu m$ , $I=2mA$ , $DN=15cm^2/s$ . -----	46
<b>Figure 4.6</b>	The time evolution of optical intensity, for (a) Without current confinement ( $sp=1\mu m$ ) (b) With current confinement ( $sp=0\mu m$ ). $Rox=1\mu m$ , $I=2mA$ , $DN=15cm^2/s$ . -----	47
<b>Figure 4.7</b>	L-I curve : the thermal effect is neglected. -----	48
<b>Figure 4.8</b>	L-I curve and its size-dependent parameters: the thermal effect is included. -----	49
<b>Figure 4.9</b>	The carrier concentration distribution represents the phenomenon of SHB for 1D(left) and 2D(right). -----	50
<b>Figure 4.10</b>	The carrier concentration in various bias currents. $Rox=2.25\mu m$ . -----	51
<b>Figure 4.11</b>	The influence of SHB on the dynamic responses of VCSELs, the time and frequence domain are included. The $sp=0\mu m$ for left-set, and $sp=1\mu m$ for right-set. For (a)(b) the influence of diffusion constant and current spreading coefficient on SHB, (c)(d) transient response, (e)(f) modulation response. $Rox=2.25\mu m$ , $I=2mA$ . -----	53
<b>Figure 4.12</b>	The influence of current spreading coefficient on the current injection profile and modulation properties. $Rox=2\mu m$ , $I=3mA$ , $DN=15cm^2/s$ . -----	54

<b>Figure 4.13</b> The thermal effect of current-dependent. $R_{ox}=4\mu m$ , $R_{th} = 5000K/W$ .	55
<b>Figure 4.14</b> The small signal modulation with different bias current without thermal effect.	56
<b>Figure 4.15</b> The small signal modulation with different size. The output power is 1mW.	56
<b>Figure 4.16</b> D factor	57

## TABLES

<b>Table 1.1</b> Degeneracy of LP modes	4
<b>Table 3.1</b> The parameters of models	24

# CHAPTER 1

## INTRODUCTION

Vertical Cavity Surface Emitting Lasers (VCSELs) are promising for applications in optical communication, optical fiber computer networks, high-density optical storage, printing, optical sensing, display system and interconnects because of their useful characteristics such as low threshold current, single longitudinal-mode operation, circular output beam with low divergence, and wafer-scale integration, etc. However, despite these advantages, VCSELs still exhibit a number of undesirable features such as the excitation of higher-order transverse modes and the undetermined polarization properties. The simple testing procedure also is one of merits of VCSELs even though the epitaxial growth of DBRs is required. This is because VCSELs allow manufacturers to carry out on-wafer testing prior to dicing and packaging so that the production cost is much lower than that of facet emitting lasers (Figure 1.1).

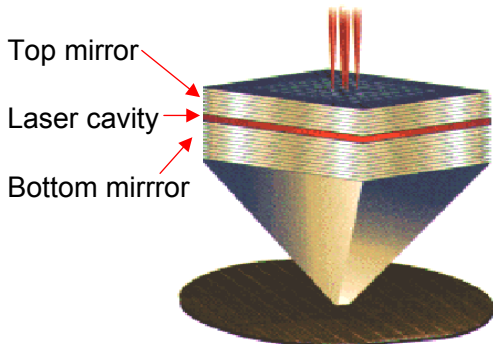


**Figure 1.1** Millions of VCSELs on a single wafer.

VCSELs are made by sandwiching a light emitting layer (i.e., a thin semiconductor of high optical gain such as quantum wells) between two highly reflective mirrors as shown in Figure 1.2. Design and fabrication of VCSEL's require an iterative process, which is extremely expensive and time-consuming. The use of simulation tools can help shorten the design cycle and speed up the process development. Laser models that are present in this work can be used to implement the simulation tools for the analysis and design of VCSELs. However, some comprehensively models, which perform sophisticated functions, are difficult to

implement and show low computational efficiency. Other simplified models exhibit high computing speed but deliver inadequate results. In 2003, Marc Xavier Jungo proposed a mathematical transformation of models based on physical and geometrical properties of VCSELs which allows removing any explicit spatial dependency from the rate equations, resulting in a numerical efficiency improved by several orders of magnitude without losing information [1].

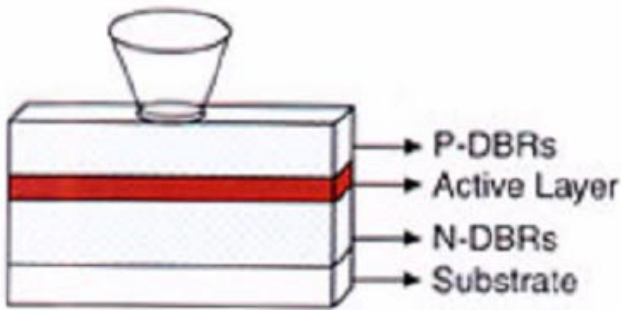


**Figure 1.2** VCSEL structure

## Thermal effect

In the simulation of VCSELs under continuous wave (CW) operation, the influence of self-heating (thermal effect) should not be avoided because of its small laser volume. In Fact, the most widely recognized limitation on the performance of VCSELs is the generation of heat inside the laser cavity. Self-heating in VCSELs can be attributed to excessive heat-source and the accumulation of heat inside the laser cavity. Excessive heat-source is due to the high series resistance (i.e., a value of few hundred ohms) of the doped DBRs, which is much greater than that of facet emitting lasers. On the other hand, heat dissipation from the laser cavity of VCSELs into the heat-sink is relatively slow when compared to that of facet emitting lasers. This is due to the high current density, high thermal resistance, as well as the junction up configuration of VCSELs. Hence, serious heat accumulation inside the laser cavity is unavoidable because of high thermal resistance and injection current density. This is why VCSELs usually operates at a higher temperature than do facet emitting lasers. The substantial increase in temperature causes the increase in threshold current density, the reduction of output optical power, and the shift of resonant frequency to the longer wavelength. As a result, the influence of thermal effect on device performance is more pronounced in VCSELs than in facet emitting lasers.

It must be noted that the investigation of VCSELs using cold cavity approximations is not realistic. This is so because most of the measurable data, such as threshold current, lasing wavelength, slope efficiency, and output power, all

depend on the operating temperature of lasers. Self-heating is due to the high thermal resistance of DBRs, which prohibits the dissipation of heat from the active layer to the heat-sink. Understanding the self-heating effect will help improve the performance of VCSELs. The theoretical study of self-heating requires information about the distribution of heat-sources and thermal resistance. The use of effective heat-source and effective thermal resistance is the simplest approach to estimate the temperature change inside the laser cavity. The effective heat-source is assumed to be located at the center of the active layer, and its magnitude is roughly equal to the difference between input electrical power and output optical power and can be expressed as

$$\frac{dT(t)}{dt} = \frac{P_{ele} - P_{out}}{C_{th}} - \frac{T(t) - T_{sub}}{R_{th}C_{th}} \quad (1-1)$$

However, the Eq.(1-1) will not provide detailed information on heat distribution in the laser cavity. The detail of Eq.(1-1) will be discussed in Chapter 3.

## Spatial Hole Burning

In order to investigate the static and dynamic properties of VCSELs, the effect of spatial hole burning (SBH) is also taken into account. Although VCSELs operate in single longitudinal mode there are often many transverse modes competing at large bias current, which can have dramatic effects on the static and dynamic behavior of VCSELs. This mode competition causes both spatial and temporal fluctuations in the intensity of the emitted light. SHB is the inhomogeneous carrier distribution due to an inhomogeneous photon distribution. In the region with a high photon density, the locally higher stimulated recombination will deplete the carriers and create a “hole” in the carrier distribution result in the decrease of gain in that hole, see Figure 1.3. This hole will reduce the lateral confinement for the main optical mode and increase the overlap with side-modes, leading to a mode-jump and multimode operation. Since the depth of the hole also varies during modulation, it will affect the dynamic response of the VCSELs. The ambipolar diffusion coefficient  $D_N$  is one of the important factors to dominate the capability of refilling the hole. It is obviously that any physical delay may degrade the high-speed performance of the VCSELs and affecting the modulation response as well [2]. As a result, for more realistic investigation (i.e. the carrier transport effect is included) the higher ambipolar diffusion coefficient is always desirable.

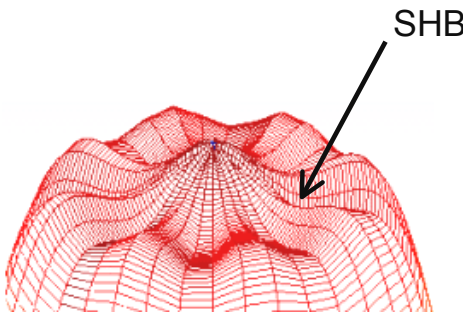


**Figure 1.3** Carrier distribution in the active region.

## Optical Modes

The transverse mode characteristics of VCSELs can be analyzed by the cylindrical dielectric waveguide theory [3], because VCSELs with cylindrical geometry have transverse confinement structures similar to that of optical fiber. Some investigation of the transverse mode characteristics of VCSELs use a full set of optical modes, including TE (transverse electric), TM (transverse magnetic, and their hybrid modes (i.e., HE and EH modes). In this paper, the properties of VCSELs with weakly index-guided structure are demonstrated. For weakly index-guided structure (i.e.,  $n_{core} \approx n_{cladding}$ ), one can transform the full set of modes into a simpler set of transverse modes, which is referred to as LP (linearly polarized) modes is given in Table 1.1. The main advantage of LP modes is that only one transverse electric component and one transverse magnetic field component are significant so that the corresponding expression of field profile can be simplified enormously. In this case, the LP mode approximation significantly simplifies the study of model characteristics of VCSELs. Therefore, the LP modes are commonly used to analyze the transverse mode characteristics in VCSELs with weakly index-guided structure.

### Composition of the lower-order linearly polarized modes

LP-mode designation	Traditional-mode designation and number of modes	Number of degenerate modes
LP <sub>00</sub>	HE <sub>00</sub> × 2	2
LP <sub>10</sub>	TE <sub>01</sub> , TM <sub>01</sub> , HE <sub>10</sub> × 2	4
LP <sub>20</sub>	EH <sub>11</sub> × 2, HE <sub>20</sub> × 2	4
LP <sub>02</sub>	HE <sub>12</sub> × 2	2
LP <sub>30</sub>	EH <sub>21</sub> × 2, HE <sub>30</sub> × 2	4
LP <sub>12</sub>	TE <sub>02</sub> , TM <sub>12</sub> , HE <sub>22</sub> × 2	4
LP <sub>40</sub>	EH <sub>31</sub> × 2, HE <sub>40</sub> × 2	4
LP <sub>22</sub>	EH <sub>12</sub> × 2, HE <sub>32</sub> × 2	4
LP <sub>03</sub>	HE <sub>13</sub> × 2	2
LP <sub>50</sub>	EH <sub>41</sub> × 2, HE <sub>50</sub> × 2	4

**Table 1.1** Degeneracy of LP modes

The modal transverse distributions are calculated by considering the VCSEL cavity as a weakly index-guided cylindrical passive waveguide. The eigenvalue equation obtained from the analysis of the scalar Helmholtz equation for the specific geometry is solved numerically, and the LP-modes are then calculated analytically [3]. The two lowest order of LP-modes accepted by a given cavity are shown in Figure 1.4. The method to obtain the optical distribution of each LP mode is introduced in chapter 3.

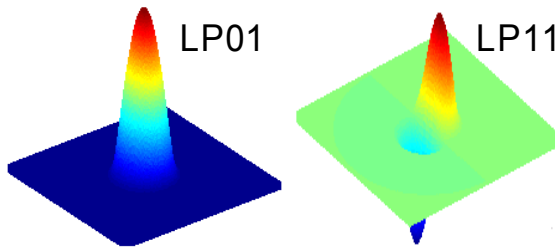


**Figure 1.4** Transverse field distribution of LP01 and LP11.

## Simulation tool- MATLAB

The programming skill is an essential part for modeling simulation, too. How to program an efficiency algorithm without losing accuracy is highly desirable. The MATLAB is one of the candidates for many simulation and numerical analysis tools due to its very efficient nature of the implemented algorithm, the required time for running a typical simulation on a standard computer (or even a laptop), is always kept within acceptable limits (typically 1min-10min). MATLAB m-files, which are readability and flexibility which are also easy to understand and modify, and MATLAB provides powerful tools for debugging and visualization and allows optimal portability, are given in Figure 1.5. In this paper, all of the outputs are implemented by MATLAB.

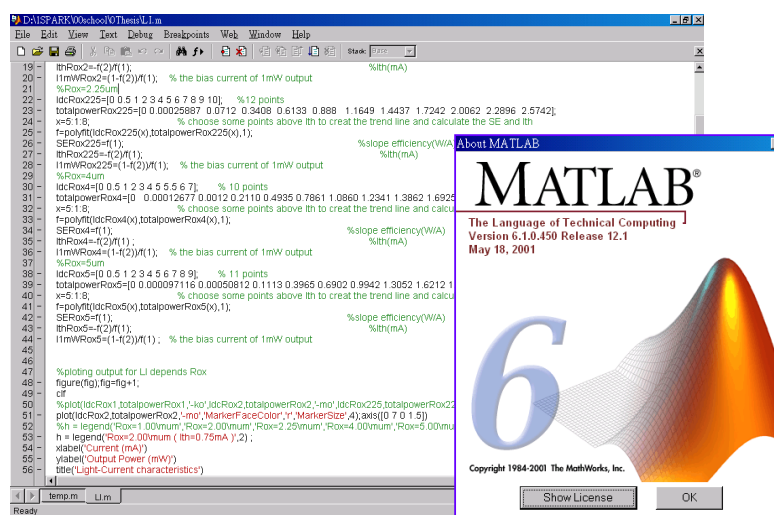


**Figure 1.5** The working environment of MATLAB.

So far, the most important effects such as thermal, SHB to the static and dynamic properties of VCSELs are simply introduced. In addition, the steady state and small-signal response of VCSEL's with different aperture sizes are also mentioned. It is found that the threshold current and light-current curves of VCSELs are determined by its cavity loss and thermal resistance, which are also size-dependent. Furthermore, small-signal analysis shows that a VCSEL with a small aperture size exhibits wider modulation bandwidth due to its high relaxation oscillation frequencies. However, the influence of parasitics effect may be considered in the high-speed application. In this paper, the transient response, mode competition, frequency response (i.e., small signal modulation), LP mode profile, carrier distribution, multimode operation, spreading current effect, thermal effect, leakage effect are investigated.

Certainly, it would be hardly possible to cover all the aspects of characteristics of VCSELs within this paper. However, the main purpose of this paper is to provide an idea and guideline about how to investigate the device properties by modeling techniques. As VCSEL's are rapidly moving into actual applications, there is a need for simple physical models to improve device performance and shorten design cycles.

This paper is organized as follows:

## Chapter 1 Introduction

The motivation of VCSEL modeling work and its application are introduced. The theoretical description of most important effects such as thermal and SHB were mentioned. The simulation tool MATLAB is also represented and its merits are explained simply.

## Chapter 2 Rate Equations

Describing the physical phenomena of all the terms regard for the rate equations and arrange all of them to a convenience formation by the reasonable assumptions. The extension of the simplest rate equations to a more complicated spatiotemporal-2D rate equations is covered. Many basic concepts of lasers can be found here.

## Chapter 3 Models and parameters

Describing the structure and materials used in this modeling. The mathematical expression of models, such as rate equations, thermal model, and LP modes

calculation methods are presented. A flow chart modeling is given in this chapter.

#### Chapter 4 Simulation results and numerical analysis

The simulation results, comparison, and explanation are illustrated. It includes the static state and dynamic responses of VCSELs, spatial hole burning, thermal effect, mode competition, carrier diffusion and spreading current effect on modulation response.

#### Chapter 5 Conclusions

# CHAPTER 2

## RATE EQUATIONS

The rate equations provide the most fundamental description of the laser. It describes the time-evolution of carrier and photon densities in a laser cavity as a function of the pump rate, material gain and parameters associated with the material properties and laser construction. In its simplest form, it consists of a pair of coupled nonlinear differential equations Eq.(2-1), one for the carrier density, and one for the photon density. Therefore it is well suited for modeling simulation. By this technique, many of properties of VCSELs can be investigated in this paper.

$$\begin{cases} \frac{dN(t)}{dt} = \frac{\eta_i I(t)}{qV_a} - \nu_g S(t)G(N, S) - \frac{N(t)}{\tau_N} \\ \frac{dS(t)}{dt} = \Gamma \nu_g S(t)G(N, S) + \beta \frac{N(t)}{\tau_N} - \frac{S(t)}{\tau_S} \\ G(N, S) = g_0 \frac{N(t) - N_{tr}}{1 + \varepsilon S(t)} \end{cases} \quad (2-1)$$

The phase does not enter into Eq.(2-1), since the optical power does not depend on the phase, it depends on the optical magnitude only. However, some effects are highly related to the laser phase, such as mode locking, injection locking and polarization switching, etc, in this situation, the phase has to be taken into account. Before proceeding further, it is important to clear up the fundamental mechanisms and assumption in the rate equations. Such as stimulated and spontaneous emission, stimulated absorption, non-radiative recombination, and so on. When referring to “carriers”, the *ambipolar assumption* is applied, that means there is no difference between electrons and holes.

### 2.1 Carrier Rate Equation

The rate of change of the electrons (or holes) density comes from electron-hole generation and recombination. And these changes must be related to the number of photons produced (for a direct bandgap semiconductor). We assume that the

electrons and holes remained confined to the active region having volume  $V_a$ . It is intuitive to obtain the basic form of carrier rate equation:

$$\begin{aligned}
 \frac{dN}{dt} &= \text{Generation - Recombination} & (2-2) \\
 &= \text{Pump} - \left( \begin{array}{l} \text{Stimulated emission} \\ - \text{Stimulated absorption} \end{array} \right) - \text{Spontaneous recombination} - \text{Non-radiative recombination} \\
 &= G_{inj} - R_{stim} - R_{spon} - R_{nonr}
 \end{aligned}$$

where  $G_{inj}$  is pumping energy,  $R_{stim}$  is stimulated recombination which is the difference between stimulated emission and stimulated absorption,  $R_{spon}$  is spontaneous emission, and  $R_{nonr}$  is non-radiative recombination. In Figure 2.1, it shows all the individual terms contribute to the carrier rate equation. Now, we will carefully examine each term as the section proceeds.

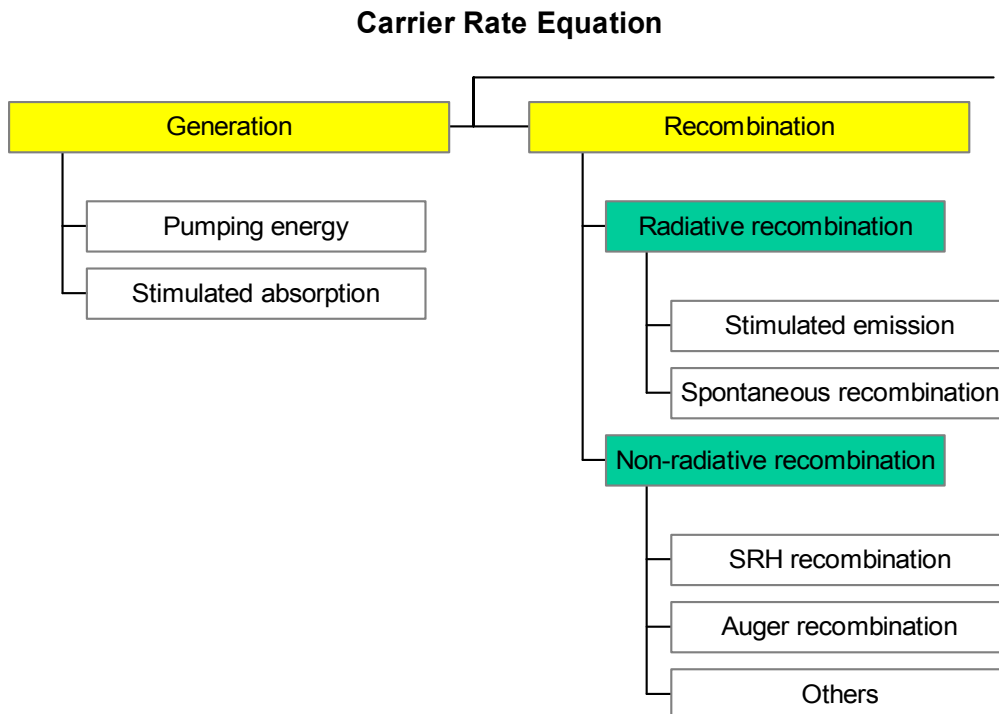


**Figure 2.1** The individual terms considered by general carrier rate equation.

## 2.1.1 Pumping Energy

The pump consists of either bias current or optical flux. The pump term describes the density of electron-hole pairs produced in the active volume  $V_a$  in

each second, which is given by

$$G_{inj} = \frac{\eta_i I(t)}{q V_a} \quad (2-3)$$

where  $G_{inj}$  is pumping current density per second (carriers/cm<sup>3</sup>/ sec),  $\eta_i$  is injection efficiency or internal quantum efficiency (ideal is 1),  $I(t)$  is injection current per second,  $q$  is the elementary charge which changes the units from coulombs to the “number of electrons”. Pump increases the number of electrons and holes in the conduction band (CB) and valence band (VB), respectively, is shown in Figure 2.2.

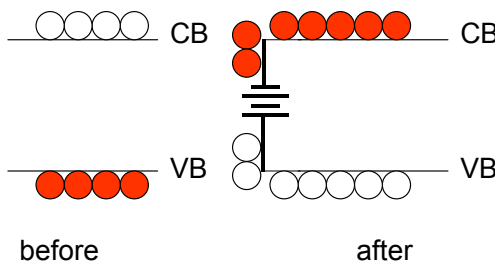


**Figure 2.2** The continuous pumping is the essential condition to reach population inversion.

The injection efficiency  $\eta_i$  represents the fraction of injected current that flow into the active region. In practical, due to the surface leakage or other carrier loss mechanisms, the  $\eta_i$  is always less than 1, it is defined by

$$\eta_i \equiv \frac{\text{carriers in active region}}{\text{total injected carriers in the device}} \quad (2-4)$$

## 2.1.2 Stimulated absorption and stimulated emission

The reason we discuss stimulated absorption and emission in the same section is due to their interaction will be used to present the concept of gain medium, it is the major part of laser device ( recall laser = *Light Amplified by the Stimulated Emission of Radiation* ). Both of stimulated absorption and stimulated emission results from stimulated recombination, therefore, need photons to conduct its process (see Figure 2.3). In contrast, the spontaneous emission does not need photons to conduct its

process, will be discussed in next section(2.1.3). According to their various physical mechanisms, please refer to [3][4][5] for further explanation, again, the main purpose of this paper is to demonstrate how to build up a device model based on well-known electro-optics theory. In the simplest way to merge stimulated absorption and emission mechanisms into to rate equations is to understand the stimulated absorption process would decrease photons number and electron-hole pairs increased. On the opposite, the stimulated emission process would multiple increase photons (photons amplified) and electron-hole pairs decreased, that's why the pumping current should maintain in a certain level to keep the emission process continuously in the active region.

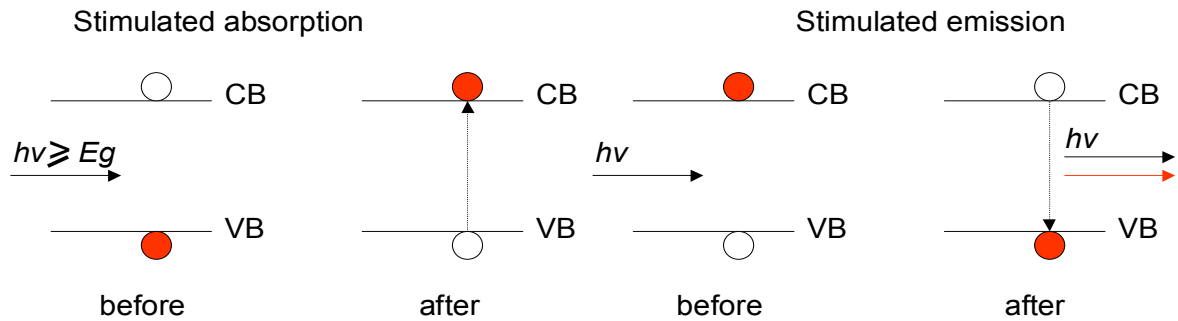


**Figure 2.3** Stimulated absorption generates more electron-hole pairs. Stimulated emission produced coherent light (same energy, phase, propagation direction, highly monochromatic).

The term  $R_{stim}$  is stimulated recombination which is the difference between stimulated emission and stimulated absorption, usually, the stimulated recombination produces more photons than them absorbed (this is one of the essential conditions for lasing, otherwise, the gain will be less than one, no amplified). The Figure 2.4 shows single photon incident on the left side of the gain medium. This photon enters the material and interacts with the carriers. Some of the processes emit photons (stimulated emission) while some of them absorb photons (absorption or sometimes called stimulated absorption) and some do nothing. It implies the gain is the ratio of output photons over the input photons. The gain describes here only the stimulated emission and absorption processes and does not include photon losses through the side of the laser or through the mirrors.

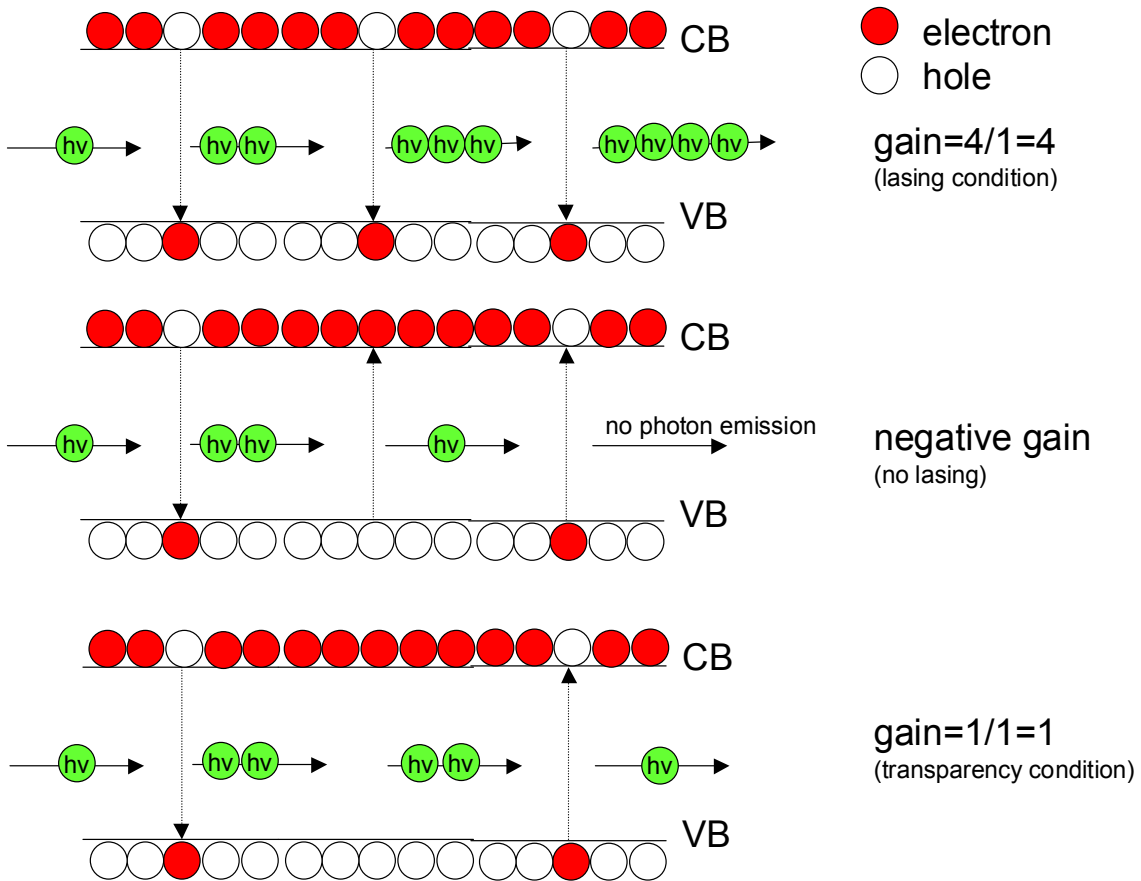


**Figure 2.4** The interaction of stimulated absorption and stimulated emission contribute the optical gain of material. The “gain” represents in this figure is just the ratio of photons that is not the same as “material gain” we will discuss later. It also presents the gain is the function of photons traveling length.

The lower one of Figure 2.4 brings up one terminology, called “material transparency”. The semiconductor material becomes “transparent” (“material transparency”) when the rate of stimulated absorption just equals the rate of stimulated emission. One incident photon produces exactly one photon in the output. The transparency density  $N_{tr}$  (number per unit volume) represents the number of excited carriers per volume required to achieve transparency. The material gain required to achieve lasing will be much larger than zero since the gain must offset other losses besides stimulated absorption (typically  $G=150 \text{ cm}^{-1}$ ). The relation between material gain and carrier density is depicted in Figure 2.5. This yields the simplest expression of material gain:

$$G(N) = g_0(N - N_{tr}) \quad (2-5)$$

where  $g_0 = \frac{dG(N)}{dN}$  is the linear gain coefficient or differential gain,  $N_{tr}$  is transparency density. In this case, we assume the photon density  $S$  is not high. Therefore, the gain curves can be approximated by a straight line at  $N_{tr}$  (refer to Figure 2.5).

When photon density is high enough, the factor  $(1+\varepsilon S)$  is taken into account. This factor accounts for nonlinear gain saturation, where  $\varepsilon$  is gain suppression coefficient. This yields another material gain expression:

$$G(N, S) = g_0 \frac{N(t) - N_{tr}}{1 + \varepsilon S(t)} \quad \text{unit: } \text{cm}^{-1} \quad (2-6)$$

In general, Eq.(2-6) is more practical than Eq.(2-5) in most case, however, we use Eq.(2-6) in our model.

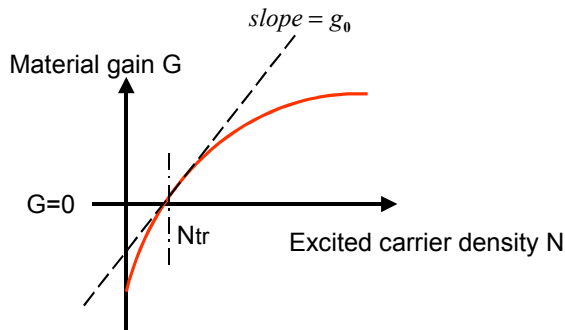


**Figure 2.5** The material gain  $G$  and differential gain  $g_0$  are the function of  $N$ .

Let's recall the beginning of this section and combine with the concept of material gain, the expression of Stimulated recombination  $R_{stim}$  can be generated:

$R_{stim} = \text{Stimulated emission} - \text{Stimulated absorption}$

$$\begin{aligned} &= G(N, S) \times S & \text{unit: } \frac{1}{\text{length}} \times \frac{1}{\text{volume}} \\ &\Rightarrow G(N, S) \times S \times v_g & \text{unit: } \frac{1}{\text{time}} \times \frac{1}{\text{volume}} \end{aligned} \quad (2-7)$$

where  $v_g$  is the group velocity of light (cm/sec). By substituting Eq.(2-6) into Eq.(2-7), we obtain

$$R_{stim} = g_0 \frac{N(t) - N_{tr}}{1 + \varepsilon S(t)} \times S(t) \times v_g \quad (2-8)$$

### 2.1.3 Spontaneous recombination

Spontaneous recombination refers to the recombination of holes and electrons without an applied optical field (i.e., no incident photons, see Figure 2.6). Spontaneous recombination produces photons by reducing the number of electrons in the conduction band and holes in the valence band. Due to it is a bimolecular recombination events, the recombination rate is proportional to “ $np$ ”, it can be written as Eq.(2-9) by ambipolar assumption ( $n=p$ ).

$$Rspn = BN^2 \quad (2-9)$$

where  $B$  is proportionality constant.

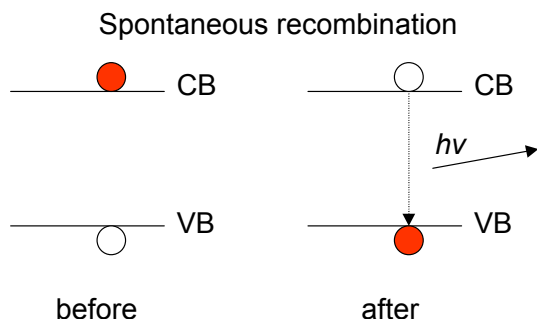


**Figure 2.6** Spontaneous recombination emits incoherent light in all directions which is a random process.

The spontaneous emission initiates laser action but decreases the efficiency of the laser. The number of photons in the lasing mode increases not only from stimulated emission but also from the spontaneous emission. Let's see how this happens. Excited carriers in the gain medium spontaneously emit photons in all directions. The wavelength range of spontaneously emitted photons cannot be confined to a narrow spectrum. Figure 2.7 compares the typical spectra for spontaneous and stimulated emission for GaAs. Some of the spontaneously emitted photons propagate in exactly the correct direction to enter the waveguide of the laser cavity. Of those photons that enter the waveguide, a fraction of them have exactly the right frequency to match that of the lasing mode. This small fraction of spontaneously emitted photons adds to the photon density  $S$  of the cavity is given as:

$$\text{Fraction of Rspn} = \beta BN^2 \quad (2-10)$$

where  $\beta$  is spontaneous recombination coefficient.

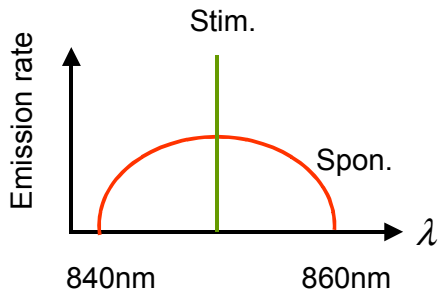


**Figure 2.7** Comparing spectra for spontaneous and stimulated emission.

## 2.1.4 Non-radiative recombination

There are two recombination mechanisms that play the major roles for non-radiative recombination (see Figure 2.8). One is Shockley-Read-Hall (SRH) recombination when an electron falls into a "trap", an energy level within the bandgap caused by the presence of a foreign atom or a structural defect. Once the trap is filled it cannot accept another electron. The electron occupying the trap, in a second step, falls into an empty valence band state, thereby completing the recombination process. One can envision this process as a two-step transition of an electron from the conduction band to the valence band or as the annihilation of the electron and hole, which meet each other in the trap. In Shockley-Read-Hall recombination, carriers are captured in trap states in the bandgap. The trap states may be created by deep level impurities (metals or transition metals) or by radiation or process induced defects (vacancies, interstitials, antisites or dislocations). We can treat SRH recombination as a monomolecular recombination and the recombination rate is proportional to "n or p", giving

$$R_{SRH} = AN \quad (2-11)$$

where  $A$  is proportionality constant.

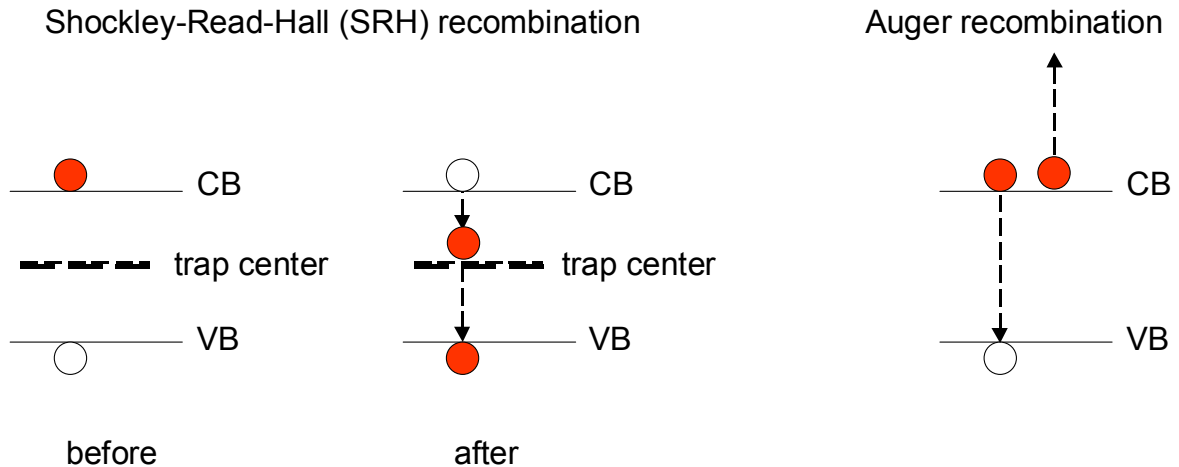


**Figure 2.8** Two non-radiative recombination mechanisms.

Another one is Auger recombination (see Figure 2.8). It involves three particles: an electron and a hole, which recombine in a band-to-band transition and give off the resulting energy to another electron or hole. The involvement of a third particle affects the recombination rate so that we need to treat Auger recombination differently from band-to-band recombination. Non-radiative Auger recombination where an electron-hole recombination instead of emitting a photon, moves a third carrier (electron or hole) to a higher energy. The third carrier dissipates its energy by heating the crystal via phonon emission. We can treat Auger recombination rate is proportional to “ $nnp$ ”, giving

$$R_{Auger} = CN^3 \quad (2-12)$$

where  $C$  is proportionality constant. By combining (2-11) and (2-12), yields

$$R_{nonr} = R_{SRH} + R_{Auger} = AN + CN^3 \quad (2-13)$$

By substituting Eq.(2-3),(2-8),(2-9) and (2-13) into Eq.(2-2) and organize all the terms, obtain carrier rate equation as:

$$\begin{aligned}
\frac{dN}{dt} &= G_{inj} - R_{stim} - R_{spon} - R_{nonr} \\
&= \frac{\eta_i I(t)}{qV_a} - g_0 \frac{N(t) - N_{tr}}{1 + \epsilon S(t)} \times S(t) \times v_g - BN^2 - (R_{SRH} + R_{Auger}) \\
&= \frac{\eta_i I(t)}{qV_a} - g_0 \frac{N(t) - N_{tr}}{1 + \epsilon S(t)} \times S(t) \times v_g - BN^2 - (AN + CN^3) \\
&= \frac{\eta_i I(t)}{qV_a} - g_0 \frac{N(t) - N_{tr}}{1 + \epsilon S(t)} \times S(t) \times v_g - (AN + BN^2 + CN^3) \\
&= \frac{\eta_i I(t)}{qV_a} - g_0 \frac{N(t) - N_{tr}}{1 + \epsilon S(t)} \times S(t) \times v_g - \frac{N}{\tau_N}
\end{aligned} \tag{2-14}$$

By defining equivalent carrier lifetime  $\tau_N^{-1} \equiv (A + BN + CN^2)$ . It implies the carrier lifetime contains the information of spontaneous recombination and non-radiative recombination.

If lasers made with “good” material,  $R_{SRH}$  term can be neglected. Also,  $R_{Auger}$  term is important for lasers (such as InGaAsP) with emission wavelengths larger than  $1 \mu m$  (small bandgap). For comparison, GaAs lasers generally emit between 800 to 860 nm. If we restrict our attention to GaAs then  $R_{Auger}$  term can be neglected. We will usually rewrite Eq.(2-10) with  $A = C = 0$  as:

$$Fraction of R_{spon} = \beta BN^2 \equiv \beta \frac{N}{\tau_N} \tag{2-15}$$

## 2.2 Photon Rate Equation

Many of the processes that decrease the carrier density  $N$  in the active volume  $V_a$  must also increase the photon density  $S$  in the modal volume  $V_m$ . Figure 2.9 shows all the individual terms contribute to the photon rate equation.

## Photon Rate Equation

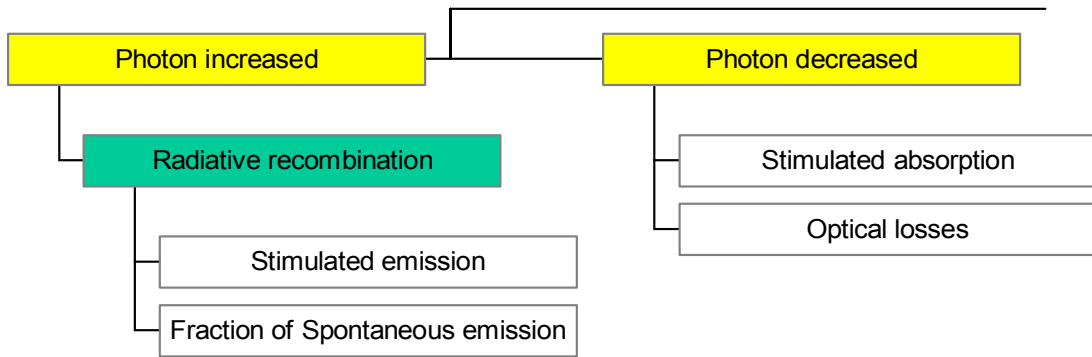


**Figure 2.9** The individual terms considered by general photon rate equation.

We can therefore write a photon rate equation as:

$$\begin{aligned}
 \frac{dS}{dt} &= \text{photon increased (radiative recombination)} - \text{photon decreased} & (2-16) \\
 &= \left( \begin{array}{c} \text{Stimulated emission} \\ + \text{Fraction of spontaneous emission} \end{array} \right) - \left( \begin{array}{c} \text{Stimulated absorption} \\ + \text{optical losses} \end{array} \right) \\
 &= \left( \begin{array}{c} \text{Stimulated emission} \\ - \text{Stimulated absorption} \end{array} \right) + \text{Fraction of spontaneous emission} - \text{optical losses} \\
 &= \Gamma(R_{stim} + \text{Fraction of Rspn}) - \text{Optical}_{loss}
 \end{aligned}$$

where the optical confinement factor  $\Gamma$  specifies the fraction of the optical mode that overlaps the gain region (active region). In other words, the confinement factor gives the percentage of the total optical energy found in the active region  $V_a$ , it can be expressed as  $\Gamma = V_a/V_m$ .

The term  $\text{Optical}_{loss}$  describes the changes of the photon density in each second by optical loss mechanisms, such as light scattering through the sidewall, free carrier absorption, mirror loss, etc, is given by

$$\begin{aligned}
 \text{Optical}_{loss} &= (\alpha_{int} + \alpha_m)S & \text{unit: } \frac{1}{\text{length}} \times \frac{1}{\text{volume}} & (2-17) \\
 &\Rightarrow (\alpha_{int} + \alpha_m)v_g S & \text{unit: } \frac{1}{\text{time}} \times \frac{1}{\text{volume}} \\
 &= \frac{S}{\tau_s}
 \end{aligned}$$

By defining  $\tau_s^{-1} = (\alpha_{\text{int}} + \alpha_m)v_g$ , where  $\tau_s$  is photon lifetime,  $\alpha_{\text{int}}$  is internal loss due to sidewalls or free carrier absorption,  $\alpha_m$  is mirror loss (both top and bottom mirrors), given

$$\alpha_m = \frac{1}{L} \ln\left(\frac{1}{\sqrt{R_1 R_2}}\right) \quad (2-18)$$

where  $L$  is cavity length,  $R_1$  and  $R_2$  are the reflectivity of top and bottom mirrors, respectively. In electromagnetic theory, if the thickness of one DBR layer is equal to  $\frac{\lambda}{4n}$ , then the highest reflectivity can be obtained, where  $n$  is refractive index for that layer. The effective reflectivity  $R$  is given

$$R = \left[ \frac{1 - \left(\frac{n_L}{n_H}\right)^{2N+1}}{1 + \left(\frac{n_L}{n_H}\right)^{2N+1}} \right]^2 \quad (2-19)$$

where  $n_L$ ,  $n_H$  are the low and high refractive indices,  $N$  is the number of periodical pairs of DBR. Figure 2.10 illustrates the thickness of DBR layer is dependent on its refractive index.

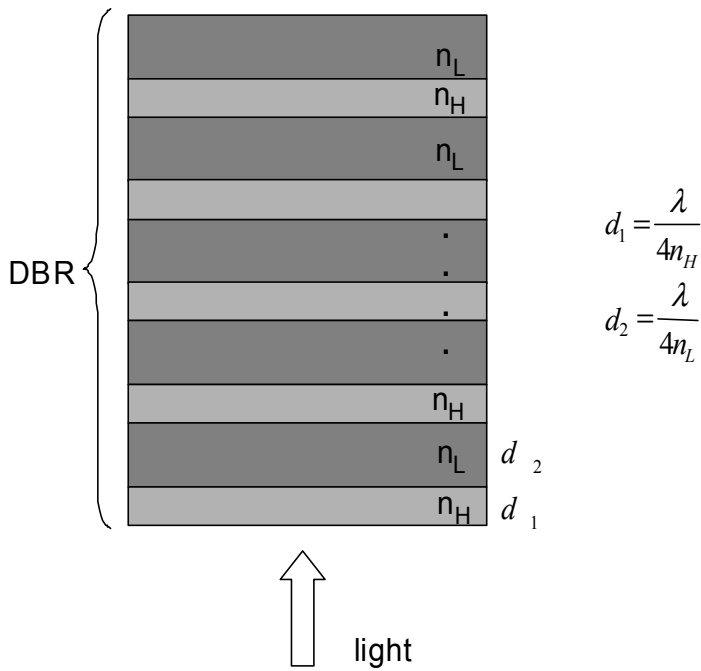


**Figure 2.10** DBR

By substituting Eq.(2-8),(2-15) and (2-17) into Eq.(2-16) and organize all the terms, obtain photon rate equation as:

$$\begin{aligned}\frac{dS}{dt} &= \Gamma(R_{stim} + Fraction\ of\ R_{spon}) - Optical_{loss} \\ &= \Gamma(g_0 \frac{N(t) - N_{tr}}{1 + \epsilon S(t)} \times S(t) \times \nu_g + \beta \frac{N}{\tau_N}) - \frac{S}{\tau_s}\end{aligned}\quad (2-20)$$

where the  $R_{SRH}$  and  $R_{Auger}$  are neglected.

For convenience, let's write the carrier rate equations Eq.(2-14) and photon rate equation Eq.(2-20) together, given Eq.(2-21) as:

$$\left\{ \begin{array}{l} \frac{dN(t)}{dt} = \frac{\eta_i I(t)}{qV_a} - \nu_g S(t) g_0 \frac{N(t) - N_{tr}}{1 + \epsilon S(t)} - \frac{N(t)}{\tau_N} \\ \frac{dS(t)}{dt} = \Gamma \nu_g S(t) g_0 \frac{N(t) - N_{tr}}{1 + \epsilon S(t)} + \Gamma \beta \frac{N(t)}{\tau_N} - \frac{S(t)}{\tau_S} \end{array} \right. \quad (2-21)$$

Radiative recombination  
 Stimulated recombination  
 Spontaneous recombination  
 +Non-radiative recombination

Carrier injection  
 Stimulated emission  
 Spontaneous emission  
 Optical losses

Eq.(2-21) is same as Eq.(2-1). It represents the general laser rate equation with all the terms and associated phenomena. It can help us to simulate the static-state and dynamic properties of VCSELs. However, the capability of Eq.(2-21) is limited due to it does not take spatial consideration into account.

Marc Xavier Jungo have proposed spatiotemporal model of VCSELs in 2003 which is a 2D (radial and azimuthal distribution), multimode, time-domain model, given in Eq.(2-22). Many of VCSELs properties can be investigated in his theoretical research [1].

$$\begin{cases} \frac{\partial N(r, \theta, t)}{\partial t} = \frac{\eta_i I(r, \theta, t)}{qV_a} - \nu_g \sum_m S_m(r, \theta, t) G_m(N, S_m) - \frac{N(r, \theta, t)}{\tau_N} + D_N \nabla^2 N(r, \theta, t) \\ \frac{\partial S(r, \theta, t)}{\partial t} = \Gamma_m \nu_g S_m(r, \theta, t) G_m(N, S_m) + \Gamma_m \beta_m \frac{N(r, \theta, t)}{\tau_N} - \frac{S_m(r, \theta, t)}{\tau_{S_m}} \\ G_m(N, S_m) = g_0 \frac{N(r, \theta, t) - N_{tr}}{1 + \frac{\epsilon}{\pi R^2} \int_{-\pi}^{\pi} \int_0^R S_m(r, \theta, t) r dr d\theta} \end{cases} \quad (2-22)$$

where  $D_N$  is ambipolar diffusion coefficient, the suffix  $m$  represents the related parameters for  $m^{th}$  mode. In generally, there are several modes contribute to laser's intensity. Each mode has its own frequency and optical profile. They play a very important role for coupling properties and other practical applications. The multimode behavior of VCSELs is dominated by the interaction of spatially inhomogeneous carrier diffusion and optical field distribution which can't be represented in Eq.(2-21). The radial and azimuthal distribution (2D) of carriers and photons for individual mode are considered in Eq.(2-22). It accounts for the phenomenon of inhomogeneous distribution of carriers and photons in the active layer and help us to understand how the spatial hole burning (SHB) and multimode operations to affect the static and dynamic properties of VCSELs. However, Eq.(2-21) is still very important for one to know how to build up the models of VCSELs base on the theory of lasers phenomenology. Due to the understanding of general laser rate equations, one can easily to translate it to Eq.(2-22). Regarding the exact mathematical derivation and formulation of the core model as well as of the advanced mechanisms can be found in [1].

# CHAPTER 3

## MODELS AND PARAMETERS

This chapter is contributed by five sections, as follows:

- 3.1 Device Structure and materials
- 3.2 Rate Equations
- 3.3 Thermal Model
- 3.4 LP modes calculation
- 3.5 Flow Chart of Algorithm.

## 3.1 Device Structure and materials

In a VCSEL, the optical cavity is defined by two distributed Bragg reflectors (DBRs) that are epitaxially grown to sandwich the gain region. The resonator axis is in the vertical (epitaxial growth) direction, so that the laser output is from the surface of the wafer. As sketched in Figure 3.1, the VCSEL optical cavity is typically a single wavelength thick, and the active medium usually has multiple quantum wells. The DBRs consist of repeating pairs of quarter-wavelength thick high and low refractive index layer. The layers composed of either monolithically grown semiconductor or dielectric materials. By placing multiple high-to-low index interfaces half a wavelength apart, the reflections from each interface add constructively to produce an effective optical reflectance of >99% for each DBR. The material parameters used in the structure can be found in Table 3.1.

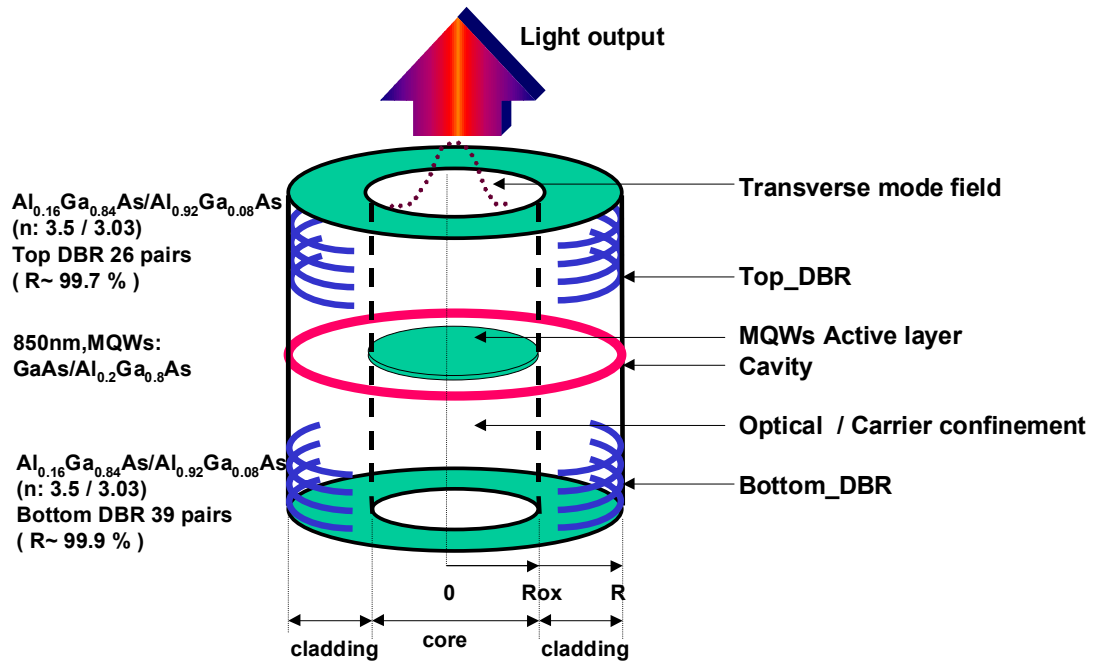


**Figure 3.1** Schematic of a cylindrical weakly index-guided structure.

Laser rate equation parameters			
symbol	parameters	value	unit
$\eta_i$	current injection efficiency	1	---
$I(t)$	injection current	5(example)	mA
$q$	elementary charge	1.602e-19	C
$V_a$	volume of the active layer	4.83e-12	cm <sup>3</sup>
$v_g$	group velocity	7.14e19	cm/s
$g_0$	linear gain coefficient or differential gain	4.53e-16	cm <sup>2</sup>
$N_{tr}$	transparency carrier density	1.85e18	cm <sup>-3</sup>
$\varepsilon$	gain compression parameter	5e-17	cm <sup>3</sup>
$\tau_N$	carrier lifetime	2.5	ns
$\tau_S$	photon lifetime	2.2	ps
$\Gamma$	optical confinement factor	0.03	---
$\beta$	spontaneous recombination coefficient	3e-5	---
$D_N$	ambipolar diffusion coefficient	15	cm <sup>2</sup> /s

Thermal model parameters			
symbol	parameter	value	unit
$\rho_m$	mass density	5.36	g/cm <sup>3</sup>
$C_p$	specific heat	0.35	J/g/C
$V_a$	volume of active layer	4.83e-12	cm <sup>3</sup>
$C_{th}$	thermal capacitance ( $C_{th} = \rho_m C_p V_a$ )	9.06e-12	J/K
$R_{th}$	thermal resistance	8000	K/W
$T_{ref}$	reference temperature for gain shrinkage	250	K
$\lambda$	actual emission wavelength	858	nm
$\lambda_p$	peak wavelength of gain spectrum	848	nm
$\Delta\Lambda$	gain profile FWHM	40	nm
Device structure parameters			
symbol	parameters	value	unit
sQW	single QW thickness	8e-7	cm
nQW	number of quantum wells	3	---
d	active region thickness ( d=sQW × nQW )	24e-7	cm
$V_c$	volume of core in active layer ( $V_c = \pi \times R_{ox}^2 \times d$ )	3.82e-13	cm <sup>3</sup>
$V_a$	volume of the active layer ( $V = \pi \times R^2 \times d$ )	4.83e-12	cm <sup>3</sup>
Leff	effective cavity length	9e-5	cm
R	cavity radius	8e-4	cm
Rox	oxide aperture radius	2.25e-4	cm
Rc	core radius(=Rox)	2.25e-4	cm
Materials parameters			
symbol	parameters	value	unit
n <sub>1</sub>	core refractive index	3.6	---
n <sub>2</sub>	cladding refractive index	3.59	---
Rt	top mirror reflectivity (26 pairs)	0.997	---
Rb	bottom mirror reflectivity (39 pairs)	0.999	---

**Table 3.1** The parameters of models

## 3.2 Rate Equations

Rate equations describe the time-evolution of carrier- and photon densities in the active layer, and are therefore well suited for simulating transient effects. In their simplest form, they consist of a pair of coupled nonlinear differential equations Eq.(3-1), one for the carrier density, and one for the photon density. Rate equations are both physics based and intuitively easy to understand. Furthermore, the spatial distributions of both the optical field and carrier density can be included as well, by adding a radial dependency of  $N$ ,  $S$  and the injected current  $I$ , and a carrier diffusion term  $D_N \nabla^2 N$ , as in Eq.(3-2), (3-3), that result in such important effects as SHB or carrier diffusion are included.

$$\begin{cases} \frac{dN(t)}{dt} = \frac{\eta_i I(t)}{qV_a} - \nu_g S(t)G(N, S) - \frac{N(t)}{\tau_N} \\ \frac{dS(t)}{dt} = \Gamma \nu_g S(t)G(N, S) + \beta \frac{N(t)}{\tau_N} - \frac{S(t)}{\tau_S} \\ G(N, S) = g_0 \frac{N(t) - N_{tr}}{1 + \epsilon S(t)} \end{cases} \quad (3-1)$$

$$\begin{cases} \frac{\partial N(r, t)}{\partial t} = \frac{\eta_i I(r, t)}{qV_a} - \nu_g \sum_m S_m(r, t)G_m(N, S_m) - \frac{N(r, t)}{\tau_N} + D_N \nabla^2 N(r, t) \\ \frac{\partial S(r, t)}{\partial t} = \Gamma_m \nu_g S_m(r, t)G_m(N, S_m) + \Gamma_m \beta_m \frac{N(r, t)}{\tau_N} - \frac{S_m(r, t)}{\tau_{S_m}} \\ G_m(N, S_m) = g_0 \frac{N(r, t) - N_{tr}}{1 + \frac{2\epsilon}{R^2} \int_0^R S_m(r, t) r dr} \end{cases} \quad (3-2)$$

$$\begin{cases} \frac{\partial N(r, \theta, t)}{\partial t} = \frac{\eta_i I(r, \theta, t)}{qV_a} - \nu_g \sum_m S_m(r, \theta, t)G_m(N, S_m) - \frac{N(r, \theta, t)}{\tau_N} + D_N \nabla^2 N(r, \theta, t) \\ \frac{\partial S(r, \theta, t)}{\partial t} = \Gamma_m \nu_g S_m(r, \theta, t)G_m(N, S_m) + \Gamma_m \beta_m \frac{N(r, \theta, t)}{\tau_N} - \frac{S_m(r, \theta, t)}{\tau_{S_m}} \\ G_m(N, S_m) = g_0 \frac{N(r, \theta, t) - N_{tr}}{1 + \frac{\epsilon}{\pi R^2} \int_{-\pi}^{\pi} \int_0^R S_m(r, \theta, t) r dr d\theta} \end{cases} \quad (3-3)$$

In Eq.(3-3), due to the distribution of  $N$  along the radial and azimuthal directions is considered, the diffusion term of Eq.(3-3) can be expressed as

$$D_N \nabla^2 N(r, \theta, t) = D_N \left[ \frac{\partial^2 N(r, \theta, t)}{\partial r^2} + \frac{1}{r} \frac{\partial N(r, \theta, t)}{\partial r} + \frac{1}{r^2} \frac{\partial^2 N(r, \theta, t)}{\partial \theta^2} \right] \quad (3-4)$$

In shortly, the Eq.(3-1) is spatial-independent, therefore, it is not suited for carrier distribution or multimode analysis. However, the steady-state and frequency response still can be demonstrated by Eq.(3-1). Eq.(3-2) only describes the radial distributions of carriers and optical field (i.e.  $N$ ,  $S$ , and  $I$  are assumed to be "doughnut shaped" in that case), and adds diffusion term to allow the investigation of SHB. Eq.(3-3) is the full model takes into account the azimuthal variation of the spatially-dependent variables. These equation represent a full 2-dimensional model, which is extremely useful for simulating effects related to imperfect coupling between laser beam and waveguide. The rate equations parameters used in these models can be found in Table 3.1.

### 3.3 Thermal Model

Heat is generated inside the active layer, due to the low electrical and thermal conductivities of the Bragg reflectivities as well as the nonradiative recombination inside the active layer. As a result, the modulation bandwidth of VCSELs is significantly reduced and the modulation signal is distorted. The corresponding thermal rate equation is given by

$$\frac{dT(t)}{dt} = \frac{P_{ele} - P_{out}}{C_{th}} - \frac{T(t) - T_{sub}}{R_{th}C_{th}} \quad (3-5)$$

where

$dT(t)$  : the temperature increased within the active layer (K)

$P_{ele}$  : electrical input power supplied to the device (K)

$P_{out}$  : output optical power in all optical modes (W)

$T(t)$  : the temperature of active layer (K)

$T_{sub}$  : ambient temperature as measured on the substrate or package

$R_{th}$  : thermal resistance (K/W)

$C_{th}$  : thermal capacitance (J/K)

Basically, it is assumed that heat is generated by the difference between the total input electrical power and the output optical power. It is noted that  $P_{ele}$  is a function of the injection current and junction voltage of the active layer. In addition, the junction voltage is a function of carrier concentration. Hence, the average temperature rise inside the VCSELs is coupled with the carrier concentration through the electrical power and optical power [6]. The Figure 3.2 depicts a schematic cross section of the VCSELs showing the overall thermal resistance ( $R_{th}$ ) and thermal capacitance ( $C_{th}$ ) of the device and Table 3.1 represents the corresponding values used in thermal model.

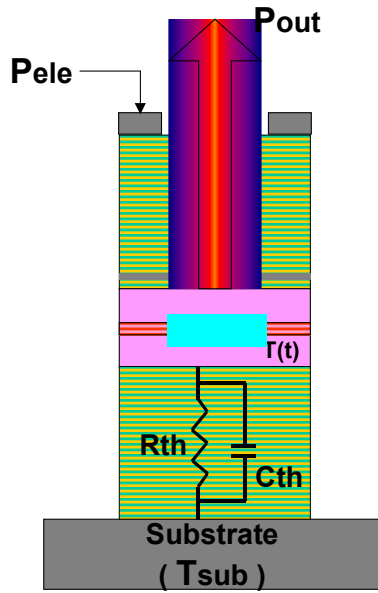


**Figure 3.2** The conceptual scheme of thermal model.

Due to the small active volume and length, VCSELs are extremely sensitive to cavity self-heating. Two different effects dominate the thermal behavior of a VCSEL cavity: gain-cavity resonance mismatch and leakage current. Gain-cavity resonance mismatch is due to the difference between the peak wavelength of the gain spectrum and the actual emission wavelength, is called gain detuning, referred to Figure 3.3, whereas carrier leakage out of the quantum wells is related to the temperature-dependency of the bandgap and quasi-Fermi levels [7].

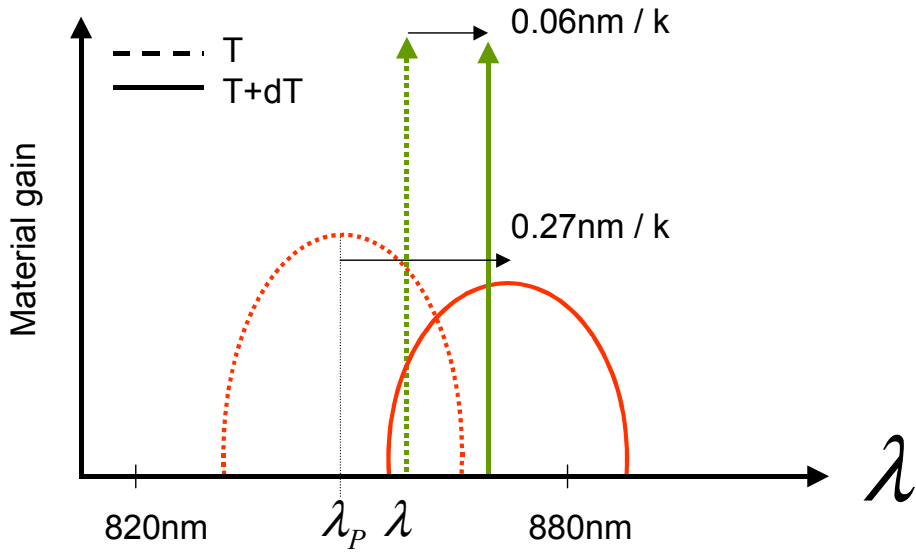


**Figure 3.3** Temperature effects on gain and cavity resonance ( Red: gain spectrum, Green: cavity resonance)

Figure 3.3 shows the influence of temperature on material gain  $G_m$  and assuming the gain peak (like  $\delta$  function) tunes at  $0.27\text{nm}/\text{k}$ , and cavity resonance tunes at  $0.06\text{nm}/\text{k}$  for a parabolic approximation, is given in Eq.(3-6). The overlap of cavity resonance with gain peak, i.e. value of gain at resonance wavelength, is the relevant gain value. However, the gain spectrum exhibits a large red shift (to long wavelength) than the cavity resonance wavelength. For that reason, VCSELs cavities are generally designed with a positive mismatch ( $\lambda - \lambda_p > 0$ ) at 300K.

$$g_0(\lambda, T) = g_0 G.T. \quad (3-6)$$

$$= g_0 \left(1 - \frac{dT}{T_{ref}}\right) \left[1 - 2\left(\frac{\lambda + 0.06dT - (\lambda_p + 0.27dT)}{\Delta\Lambda}\right)\right]^2$$

where  $g_0(\lambda, T)$  is temperature-dependent linear gain coefficient and material gain  $G_m \propto g_0(\lambda, T)$ ,  $G.T.$  is thermal gain coefficient and  $<1$  usually,  $T_{ref}$  is a fitting parameter describing the temperature-induced shrinking of gain peak value,  $\lambda$  is actual emission wavelength,  $\lambda_p$  is the peak wavelength of gain spectrum,  $\Delta\Lambda$  is gain profile FWHM (Full Width Half Maximum). The  $\Delta\Lambda$  is assumed temperature-independent, however, it is not rigorous assumption. The corresponding parameters used in these models can be found in Table 3.1.

The leakage current from quantum wells is given as

$$I_{leak} = I_0 \exp\left(-\frac{E_g(T) - \Delta E_{fcv}(N, T)}{k_B T}\right) \quad (3-7)$$

where  $I_0$  is a fitted leakage coefficient,  $E_g(T)$  is bandgap of confinement layer,  $\Delta E_{fcv}(N, T)$  is quasi-Fermi level separation in the active layer by voltage applied,  $k_B$  is Boltzmann constant. The derivation and reformulation of Eq.(3-7) can be found in [7].

## 3.4 LP modes calculation

Transverse mode characteristic of VCSELs can be analyzed by the cylindrical dielectric waveguide theory, because VCSELs with cylindrical geometry have transverse confinement structures similar to that of the optical fiber. For cylindrical dielectric waveguide with a very small refractive index difference between the core and the cladding, (i.e., weakly guiding,  $n_1 \approx n_2$  or  $\Delta \ll 1$ ) is valid for most fibers of practical interest. In this case, it allows use of the so-called weakly guiding approximation. In this approximation, the transverse field components are assumed to be essentially linearly polarized. In general, it is convenient to represent the monochromatic wave in terms of complex wavefunction  $U(\mathbf{r}, t)$ , may be written in the form

$$U(\mathbf{r}, t) = U(\mathbf{r}) \exp(j\omega t) \quad \text{complex wavefunction (3-8)}$$

where  $U(\mathbf{r})$  is complex amplitude, which is time-independent,  $\omega = 2\pi\nu$  is angular frequency (rad/s),  $\nu$  is frequency (Hz). The Eq.(3-8) must satisfy the scalar wave equation,

$$\nabla^2 U - \frac{1}{c^2} \frac{\partial^2 U}{\partial t^2} = 0 \quad \text{scalar wave equation (3-9)}$$

where  $c$  is the speed of light in the medium,  $U$  can be a complex wavefunction. By substituting Eq.(3-8) into the Eq.(3-9), yielding the differential equation, so called Helmholtz equation, which is a time-independent wave equation. Each component of

the electric and magnetic fields must satisfy the Helmholtz equation,

$$\nabla^2 U(\mathbf{r}) + k^2 U(\mathbf{r}) = 0 \quad \text{Helmholtz equation (3-10)}$$

where  $k = nk_0 = n(2\pi/\lambda_0)$  is the wavenumber of wave propagates through a medium with refractive index  $n$ . The  $k_0$ ,  $\lambda_0$  are the wavenumber and wavelength of free space ( $n = 1$ ), respectively.  $\nabla^2$  is Laplacian operator. For cylindrical coordinates, it is given as

$$\nabla^2 = \frac{\partial^2}{\partial r^2} + \frac{1}{r} \frac{\partial}{\partial r} + \frac{1}{r^2} \frac{\partial^2}{\partial \phi^2} + \frac{\partial^2}{\partial z^2} \quad \text{Laplacian operator (3-11)}$$

Rewriting Eq.(3-10) by substituting Eq(3-11), the Helmholtz equation of cylindrical coordinate system can be obtained as

$$\frac{\partial^2 U(\mathbf{r})}{\partial r^2} + \frac{1}{r} \frac{\partial U(\mathbf{r})}{\partial r} + \frac{1}{r^2} \frac{\partial^2 U(\mathbf{r})}{\partial \phi^2} + \frac{\partial^2 U(\mathbf{r})}{\partial z^2} + n^2 k_0^2 U(\mathbf{r}) = 0 \quad (3-12)$$

The optical intensity  $I(\mathbf{r})$  of a monochromatic wave is the absolute square of its complex amplitude is determined by

$$I(\mathbf{r}) = |U(\mathbf{r})|^2 \quad \text{optical intensity (3-13)}$$

As a result, the intensity of a monochromatic wave does not vary with time.

In general, applying variable separated and assuming the complex amplitude  $U(\mathbf{r})$  as

$$\begin{aligned} U(\mathbf{r}) &= U(r, \phi) \exp(-j\beta z) \\ &= R(r) \Phi(\phi) \exp(-j\beta z) \end{aligned} \quad \text{complex amplitude (3-14)}$$

where  $\beta$  is propagation constant.

Substituting Eq(3-14) into Eq(3-12) to obtain

$$\frac{r^2}{R(r)} \frac{d^2 R(r)}{dr^2} + \frac{r}{R(r)} \frac{dR(r)}{dr} + r^2 (n^2 k_0^2 - \beta^2) = -\frac{1}{\Phi(\phi)} \frac{d^2 \Phi(\phi)}{d\phi^2} \quad (3-15)$$

The left-hand side of Eq.(3-15) depends only on  $r$ , whereas the right-hand side

depends only on  $\phi$ . Since  $r$  and  $\phi$  vary independently, it must follow that each side of Eq.(3-15) must be equal to a constant. Defining the constant as  $l^2$ , Eq.(3-15) separates into the following two equations:

$$\left\{ \frac{d^2\Phi(\phi)}{d\phi^2} + l^2\Phi(\phi) = 0 \right. \quad (3-16)$$

$$\left. \frac{d^2R(r)}{dr^2} + \frac{1}{r} \frac{dR(r)}{dr} + (n^2 k_0^2 - \beta^2 - \frac{l^2}{r^2})R(r) = 0 \right. \quad (3-17)$$

Bessel's differential equation

where  $l = 0, 1, 2, 3, \dots$  (Negative values of  $l$  correspond to the same field distribution.). Eq(3-17) is called Bessel's differential equation due to its solution is the form of Bessel function. The constant  $l$  is known as the angular or azimuthal mode number.

The solution of Eq.(3-16) is

$$\Phi(\phi) = \begin{cases} \cos(l\phi + \alpha) \\ \sin(l\phi + \alpha) \end{cases} \quad (3-18)$$

where  $\alpha$  is a constant phase shift and assume its value is zero.

To solve Eq.(3-17), one need to the know the requirement of wave is guided in the fiber. For step index fiber, the wave is guided if the  $n_1 k_0 > \beta$  in the core and  $n_2 k_0 < \beta$  in the cladding,  $n_1$  and  $n_2$  represent the refractive index in the core and cladding, respectively. Eq(3-17) may then be written in the core and cladding separately:

$$\left\{ \begin{array}{ll} \frac{d^2R(r)}{dr^2} + \frac{1}{r} \frac{dR(r)}{dr} + (n_1^2 k_0^2 - \beta^2 - \frac{l^2}{r^2})R(r) = 0, & 0 < r < a \text{ (core)} \\ \frac{d^2R(r)}{dr^2} + \frac{1}{r} \frac{dR(r)}{dr} + (n_2^2 k_0^2 - \beta^2 - \frac{l^2}{r^2})R(r) = 0, & r > a \text{ (cladding)} \end{array} \right. \quad (3-19)$$

where  $a$  is core radius.

To simplify the equation above, it is convenient to define

$$\left\{ \begin{array}{l} X^2 \equiv (n_1^2 k_0^2 - \beta^2)a^2 \\ Y^2 \equiv (\beta^2 - n_2^2 k_0^2)a^2 \end{array} \right. \quad (3-20)$$

and obtain V parameter as

$$\begin{aligned}
V &= \sqrt{X^2 + Y^2} \\
&= k_0 a \sqrt{n_1^2 - n_2^2} \\
&= \frac{2\pi}{\lambda_0} a (N.A.)
\end{aligned} \tag{3-21}$$

where  $N.A. = \sqrt{n_1^2 - n_2^2}$  is numerical aperture of a step-index fiber.  $V$  is an important parameter that governs the number of modes of fiber and their propagation constants. It is important to remember that for the wave to be guided,  $X$  must be smaller than  $V$ .

Substituting Eq.(3-20) into Eq.(3-19), leading to

$$\frac{d^2 R(r)}{dr^2} + \frac{1}{r} \frac{dR(r)}{dr} + \left( \frac{X^2}{a^2} - \frac{l^2}{r^2} \right) R(r) = 0, \quad 0 < r < a \text{ (core)} \tag{3-22}$$

$$\frac{d^2 R(r)}{dr^2} + \frac{1}{r} \frac{dR(r)}{dr} - \left( \frac{Y^2}{a^2} + \frac{l^2}{r^2} \right) R(r) = 0, \quad r > a \text{ (cladding)} \tag{3-23}$$

Ordinary Bessel's Eq.

Modified Bessel's Eq.

Eq.(3-22) and Eq.(3-23) are the ordinary and modified form of Bessel's equation, respectively. The solutions of Eq.(3-22) and Eq.(3-23) are the family of Bessel functions:

$$R(r) = \begin{cases} AJ_l\left(\frac{Xr}{a}\right) + BY_l\left(\frac{Xr}{a}\right) & 0 < r < a \text{ (core)} \\ CI_l\left(\frac{Yr}{a}\right) + DK_l\left(\frac{Yr}{a}\right) & r > a \text{ (cladding)} \end{cases} \tag{3-24}$$

where  $A, B, C, D$  are arbitrary constants.  $J_l$  is ordinary Bessel function of the first kind and order  $l$ .  $Y_l$  is ordinary Bessel function of the second kind and order  $l$ .  $I_l$  is modified Bessel function of the first kind and order  $l$ .  $K_l$  is modified Bessel function of the second kind and order  $l$ . About more detailed discussions of Bessel function properties can be found in [8].

At  $r \rightarrow 0$  in the core, the solution  $Y_l$  has to be rejected due to its divergence. At  $r \rightarrow \infty$  in the cladding, the solution  $I_l$  has to be rejected due to its divergence. This results in the bounded solutions of Eq.(3-22) and Eq.(3-23):

$$R(r) = \begin{cases} AJ_l\left(\frac{Xr}{a}\right), & 0 < r < a \text{ (core)} \\ DK_l\left(\frac{Yr}{a}\right), & r > a \text{ (cladding)} \end{cases} \tag{3-25}$$

Figure 3.4 and Figure 3.5 depict the behavior of  $J_l$  and  $K_l$ .

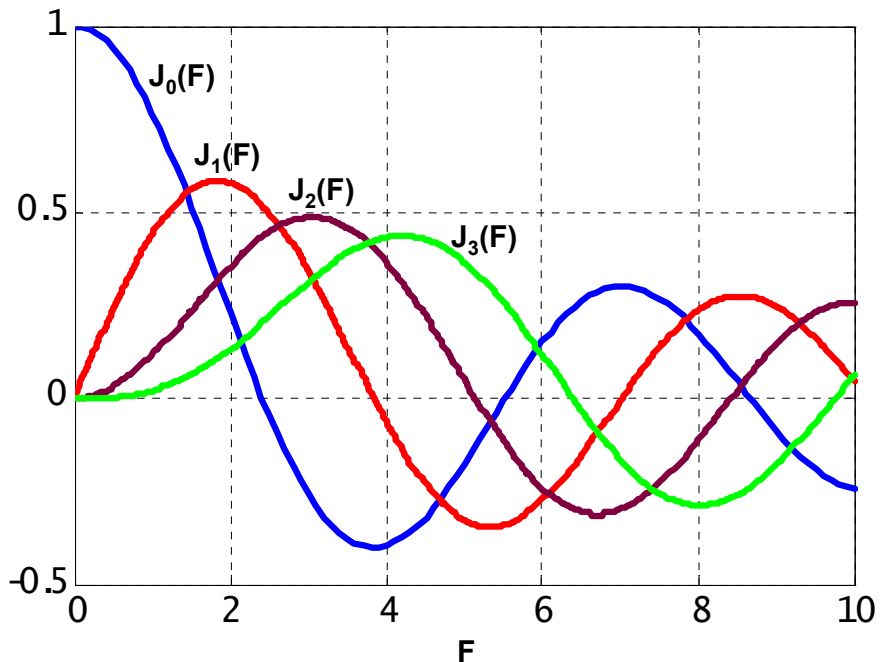


**Figure 3.4** The ordinary Bessel function of the first kind  $J_l$  and order  $l=0,1,2,3$ .

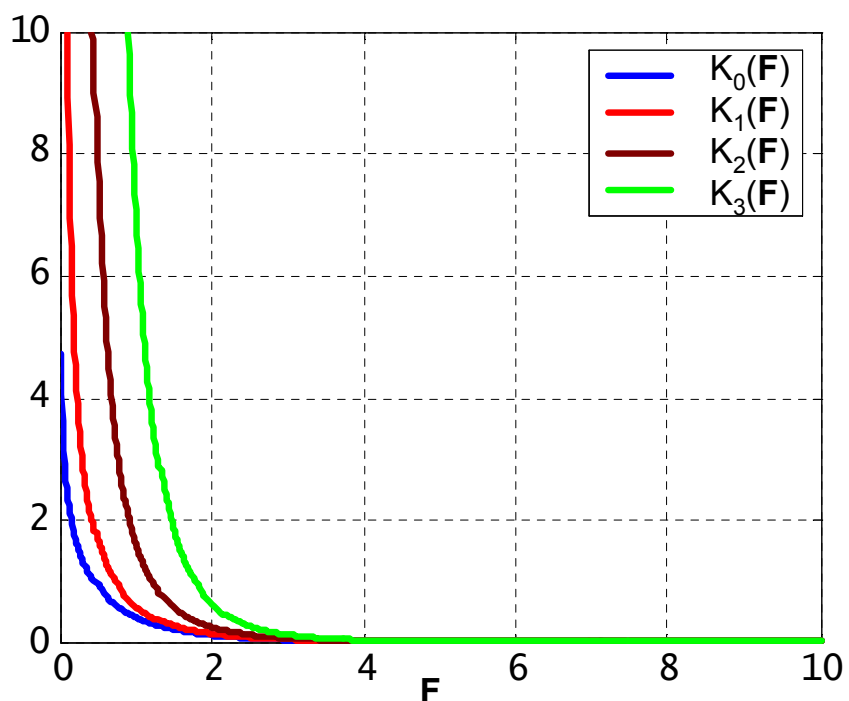


**Figure 3.5** The modified Bessel function of the second kind  $K_l$  and order  $l=0,1,2,3$ .

Substituting Eq.(3-18) and Eq.(3-25) into Eq.(3-14), and obtain the complete solution for  $U(\mathbf{r})$  is

$$U(\mathbf{r}) = R(r)\Phi(\phi)\exp(-j\beta z) \\ = \begin{cases} AJ_l\left(\frac{Xr}{a}\right)\begin{bmatrix} \cos(l\phi) \\ \sin(l\phi) \end{bmatrix}\exp(-j\beta z), & 0 < r < a \text{ (core)} \\ DK_l\left(\frac{Yr}{a}\right)\begin{bmatrix} \cos(l\phi) \\ \sin(l\phi) \end{bmatrix}\exp(-j\beta z), & r > a \text{ (cladding)} \end{cases} \quad (3-26)$$

Due to the refractive indices  $n_1 \approx n_2$  for weakly-guiding waveguide, the longitudinal components of the electric and magnetic fields are then much weaker and usually negligible in comparison to the corresponding transverse components [9]. Thus, the transverse dependence of the modal field is given by

$$\psi(r, \phi) = R(r)\Phi(\phi) \\ = \begin{cases} \frac{A'}{J_l(X)}J_l\left(\frac{Xr}{a}\right)\begin{bmatrix} \cos(l\phi) \\ \sin(l\phi) \end{bmatrix}, & 0 < r < a \text{ (core)} \\ \frac{A'}{K_l(Y)}K_l\left(\frac{Yr}{a}\right)\begin{bmatrix} \cos(l\phi) \\ \sin(l\phi) \end{bmatrix}, & r > a \text{ (cladding)} \end{cases} \Rightarrow \mathbf{LP}_{lm} \quad (3-27)$$

where  $A'$  is arbitrary constant, and the relations  $A = \frac{A'}{J_l(X)}$  and  $D = \frac{A'}{K_l(Y)}$  have been used to maintain the continuity at  $r = a$ . The subscripts on  $\mathbf{LP}_{lm}$  refer to the  $l_{th}$  order and  $m_{th}$  rank, where  $l = 0, 1, 2, \dots$  and is associated with the circular functions  $\cos(l\phi)$  or  $\sin(l\phi)$ ;  $m = 1, 2, 3, \dots$  which identifies the successive roots of Eq.(3-28) in below.

Assuming  $\psi(r, \phi)$  is continuous in the core-cladding interface, and has a continuous derivative  $\frac{\partial \psi(r, \phi)}{\partial r}$  at  $r = a$ . To satisfy these two conditions, the eigenvalue equation is obtained:

$$X \frac{J_{l+1}(X)}{J_l(X)} = Y \frac{K_{l+1}(Y)}{K_l(Y)} \quad \text{or} \quad X \frac{J_{l-1}(X)}{J_l(X)} = -Y \frac{K_{l-1}(Y)}{K_l(Y)} \quad (3-28)$$

Note that  $J_{-l}(X) = (-1)^l J_l(X)$  and  $K_{-l}(Y) = K_l(Y)$ , so that if  $l$  is replaced with  $-l$ ,

the equation remains unchanged.

The eigenvalue equation Eq.(3-28) may be solved graphically by plotting its right- and left-hand sides versus  $X$  and finding the intersections. As demonstrated in Figure 3.6 for  $l=0$ ,  $V=6.9906$ , it is readily to find the two roots for  $X$ , which indicated for  $m=1$  and  $m=2$ , respectively. Figure 3.7 represents  $l=0,1,2,3,4$ ,  $V=6.9906$  and their associated  $X$  roots and  $m^{th}$ . The derivation of LP modes from Figure 3.7 is shown in Figure 3.8 by using Eq.(3-27), the azimuthal factor is not considered in this case.

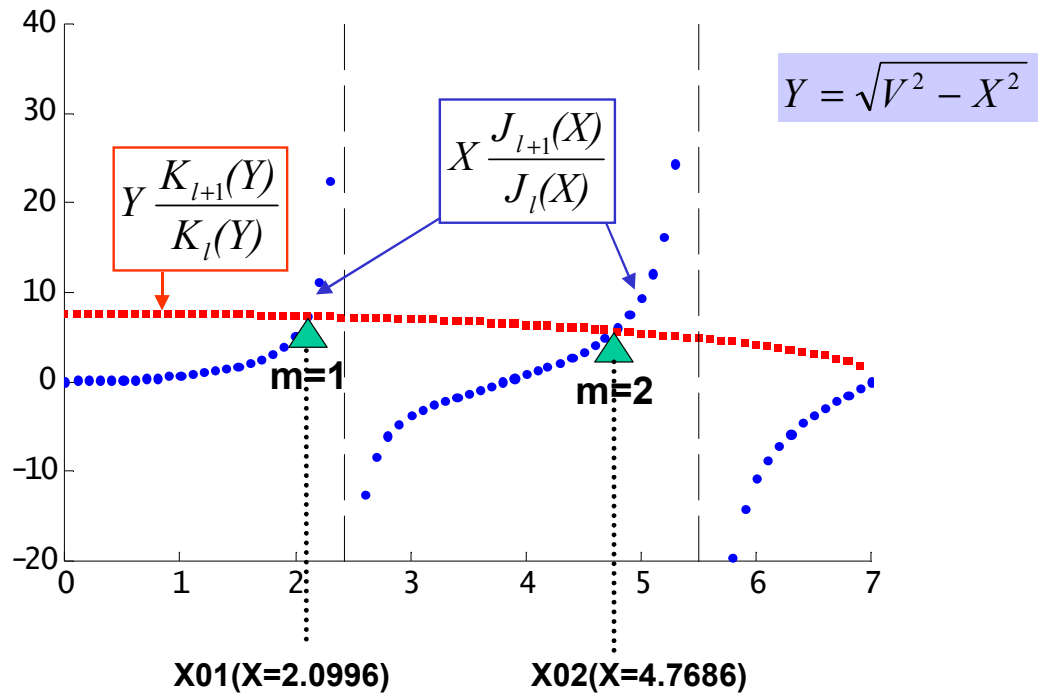


**Figure 3.6** The graphical solution of  $m^{th}$  of  $l=0$ .

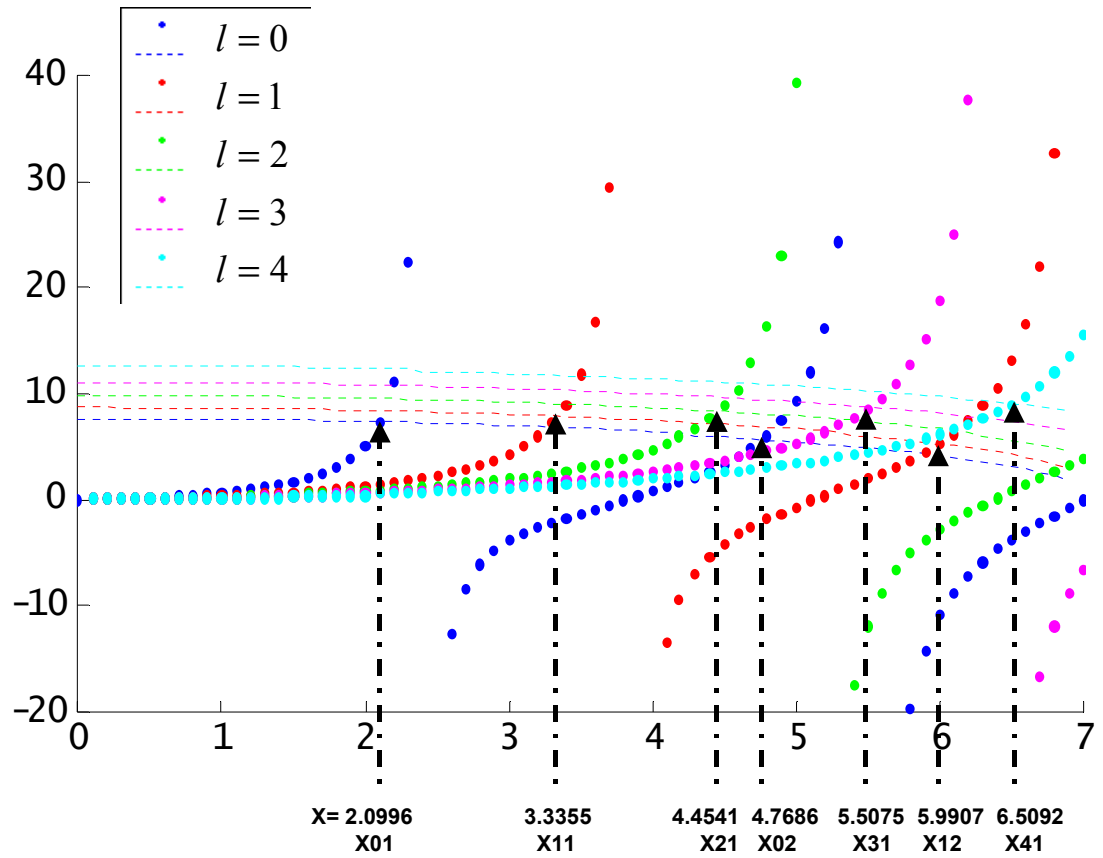


**Figure 3.7**  $l=0,1,2,3,4$ ,  $V=6.9906$  and their associated  $X$  roots and  $m^{\text{th}}$ .

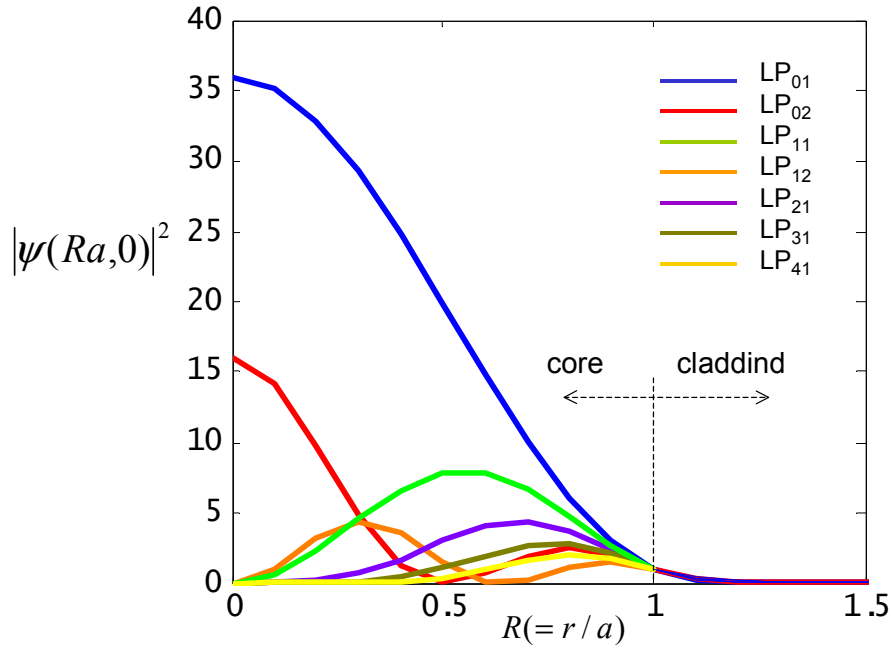


**Figure 3.8** The 1-D intensity radial distribution of various LP modes. Assuming  $A'=1$ ,  $\cos(l\phi)$  and  $\sin(l\phi)$  factors are not taken into account.

Figure 3.9, 3.10, 3.11 are the 2-D profile of four lower LP modes, they are the fully solution of Eq.(3-27). It is noted that the polarization of electric and magnetic fields are not represented here.

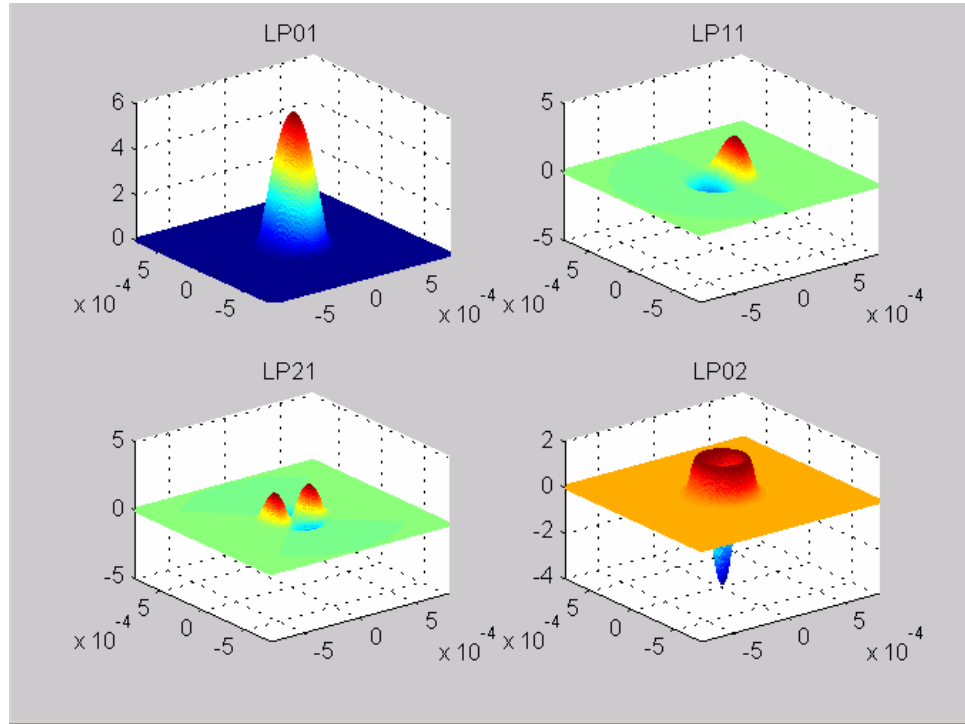


**Figure 3.9** The field distribution of four lower LP modes with  $\cos(l\phi)$  term.

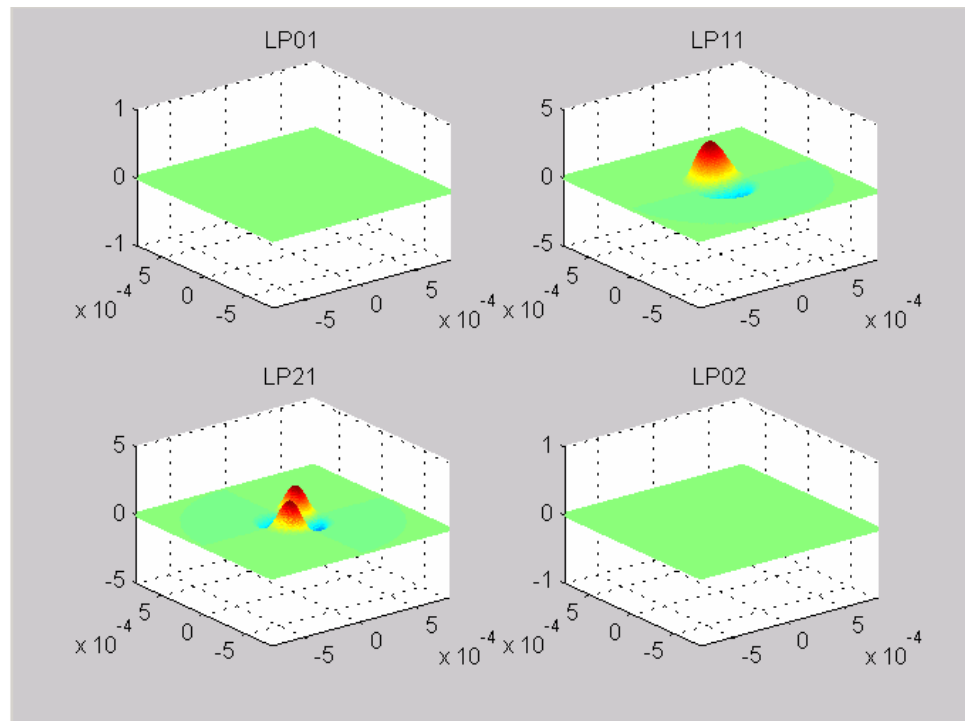


**Figure 3.10** The field distribution of four lower LP modes with  $\sin(l\phi)$  term. It is obviously there is no  $\sin$  contribution for  $\mathbf{LP}_{0m}$  modes.

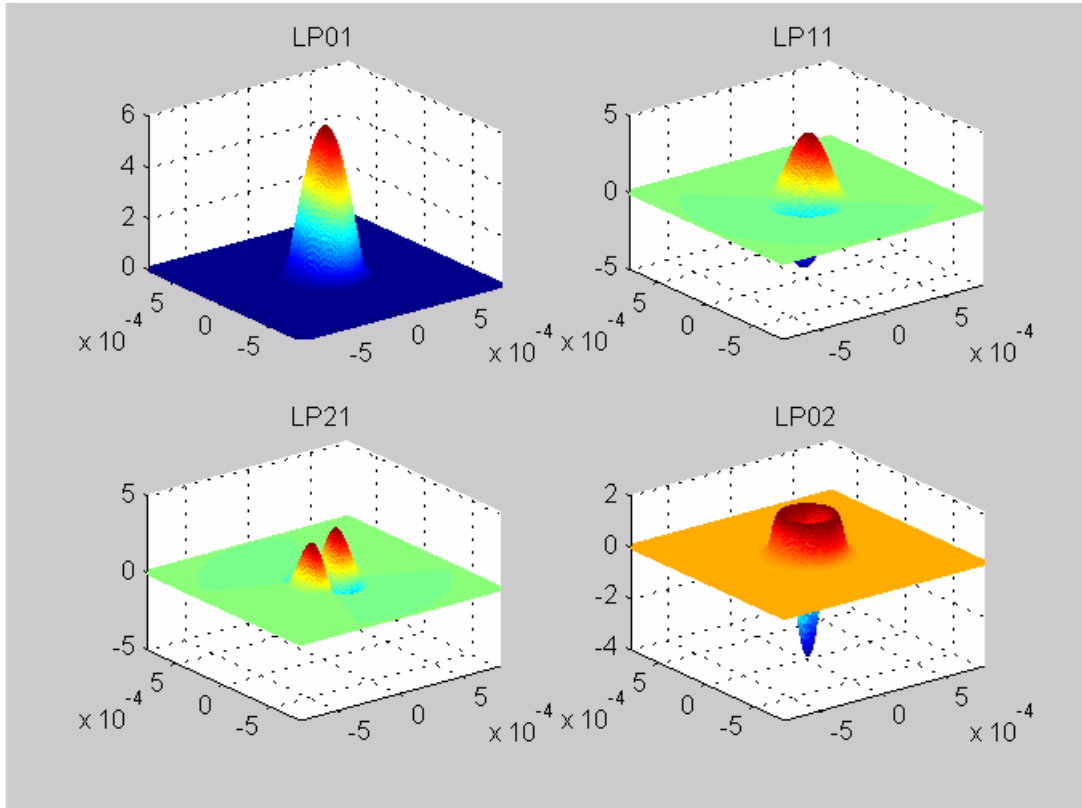


**Figure 3.11** The field distribution of four lower LP modes with  $\cos(l\phi)$  and  $\sin(l\phi)$  term.

It is convenient to define the normalized propagation constant  $b$  as

$$b \equiv \frac{(\beta/k_0)^2 - n_2^2}{n_1^2 - n_2^2} \quad (3-29)$$

$$= \frac{Y^2}{V^2}$$

and depict the universal curves is shown in Figure 3.12. For a given step index fiber and a given operating wavelength, the  $V$  parameter or normalized frequency is then calculated by Eq.(3-21) readily. According to Figure 3.12, once  $V$  is given, the value of  $b$  and  $\beta$  for each LP mode can be denoted as  $b_{lm}$  and  $\beta_{lm}$ . This method can be implemented in multi-mode operation analysis of photon rate equation.

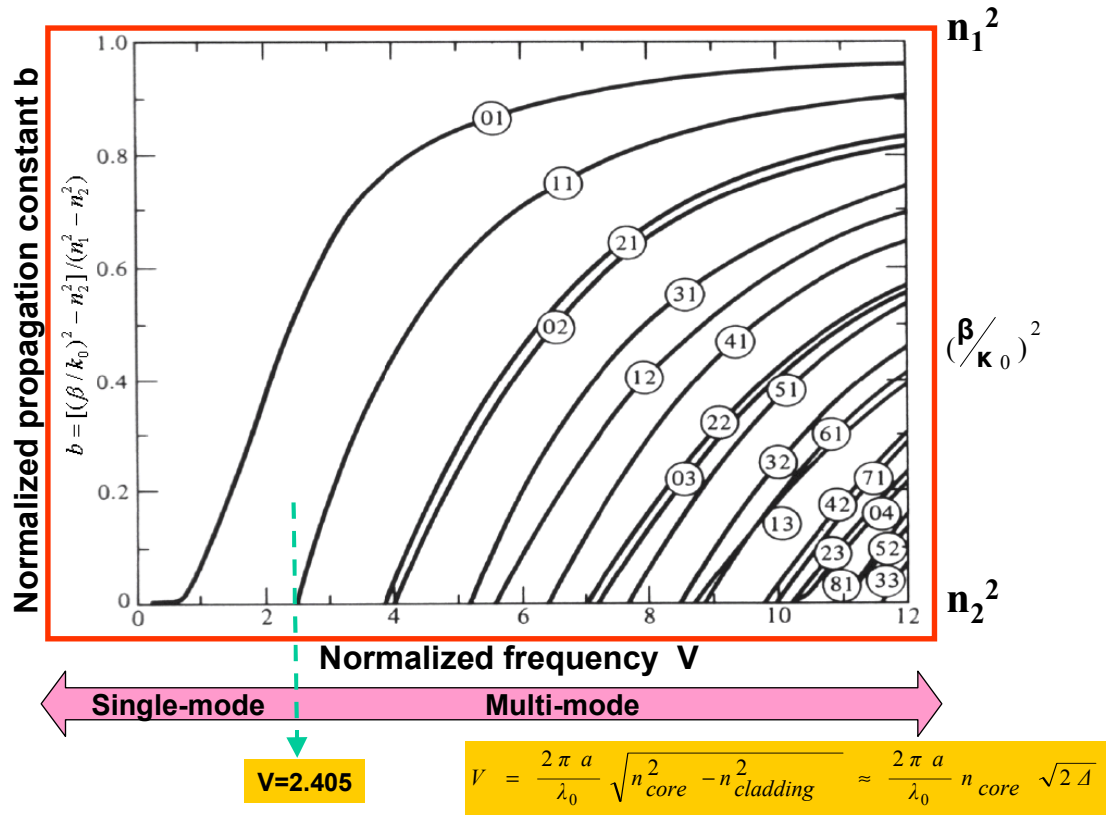


**Figure 3.12** Variation of the normalized propagation constant  $b$  with normalized frequency  $V$  for a step index fiber corresponding to various LP modes. For  $V < 2.405$ , there is only one guided mode –namely,  $\text{LP}_{01}$  mode. The cutoff frequencies of  $\text{LP}_{0,m+1}$  and  $\text{LP}_{2,m}$  are the same [9].

## 3.5 Flow Chart of Algorithm

An accurate, efficient and consistent modeling simulation relies on the design of flow chart algorithm. Such simulation enables us of better understanding the physical phenomena take place inside a VCSEL volume during its operation of many nonlinear and mutual interactions. Therefore, it is helpful to identify the parameters that are crucial for efficient laser performance and finding methods of improving. In advanced VCSEL models, all material and structure parameters should be functions of local material compositions. Additionally, physical phenomena taking place during the operation of a laser diode are mutually interrelated. Therefore, comprehensive simulation of laser diode operation needs a self-consistency part that including many important interrelations between individual phenomena. An advanced and integrated tool should be constituted in studying all aspects of VCSEL performance in the whole complexity of all interrelated physical phenomena, and used to examine VCSEL degradation processes. In fact, being a mixture of many various physical phenomena that are difficult to determine and interrelations are difficult to describe. It may be also helpful in finding an optimal VCSEL design for a given, specified applications. The most important connections between electrical, optical, and thermal phenomena are shown in Figure 3.13.

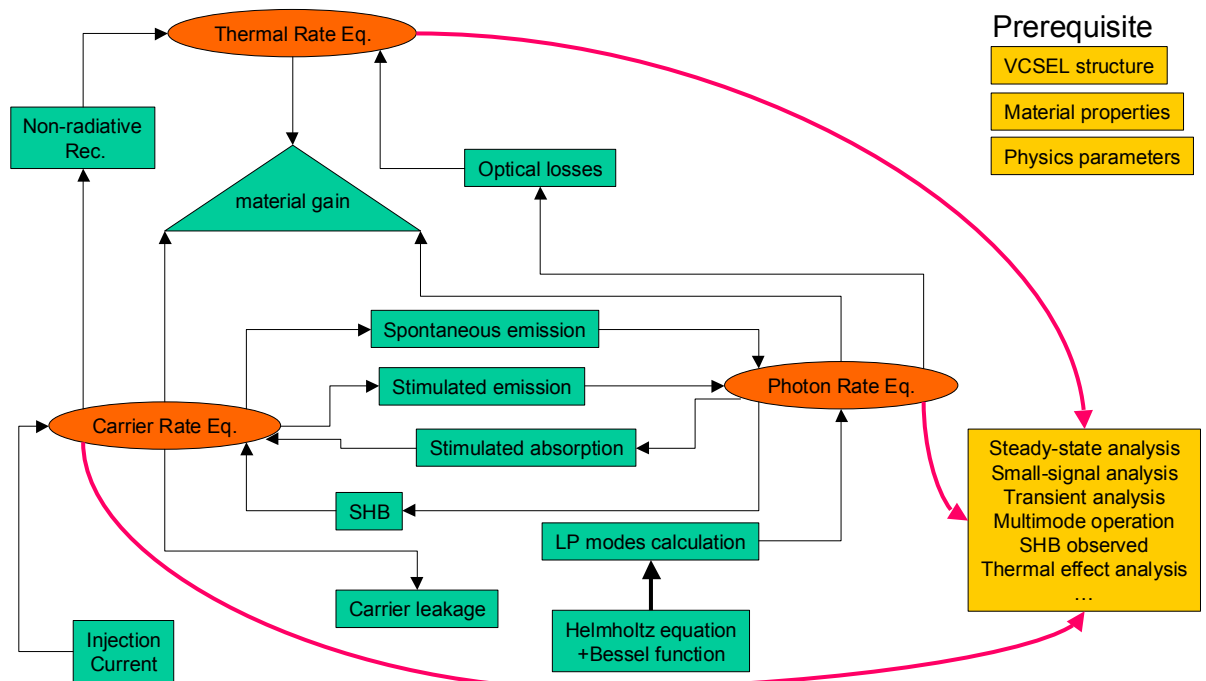


**Figure 3.13** The most important interrelationship between individual physical process.

# CHAPTER 4

## SIMULATION RESULTS AND NUMERICAL ANALYSIS

In this chapter, many simulation results regarding to the VCSELs characteristics are studies and divided into five sessions as follows.

- 4.1 The transient response of output power
- 4.2 L-I curve
- 4.3 Spatial Hole Burning
- 4.4 Thermal effect
- 4.5 Small Signal Modulation

### 4.1 The transient response of output power

The transient response of VCSELs is shown in Figure 4.1. It is observed that the output power exhibits damped oscillation and settles down for less than 1.5ns. The short term fluctuations in the intensity of the light when the laser is just turned on is called “relaxation oscillations”. Such relaxation oscillations are due to an intrinsic resonance in the laser dynamics, in which the energy stored in the system oscillates back and forth between the electron and photon populations. When power is applied to the laser the upper energy state population builds up until an inversion occurs and lasing can commence. However, lasing can deplete the upper energy state very quickly and if pumping isn't quite fast enough lasing will momentarily stop. Very soon afterwards it will start again as the pump builds up a population inversion again. The short turn-on delay time and quickly stabilized are expected. It is noted that the damping of these oscillations is dependent on non-linear gain and nonradiative recombination. The natural frequency of relaxation oscillations is in the GigaHertz

range and plays an important role in determining the dynamic response of the laser. The damped relaxation oscillation frequency is not only dependent on the laser structure, but also varies with the current injection. The higher current injection represents the shorter turn-on delay, higher output power and faster damped oscillation is shown in Figure 4.1.

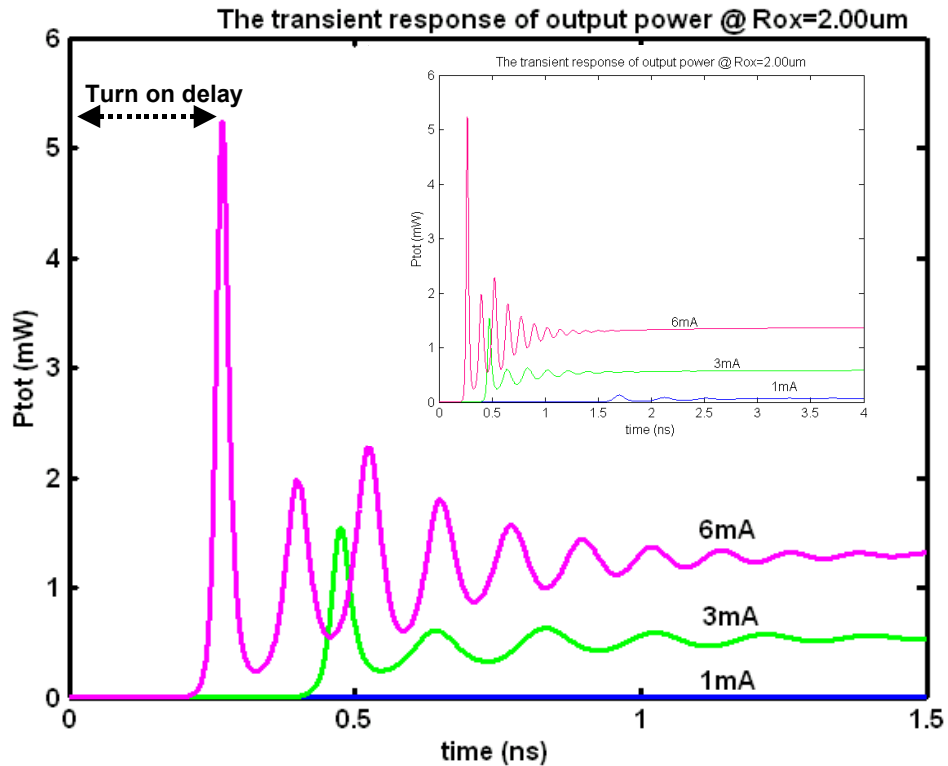


**Figure 4.1** The transient response of VCSELs with 6mA, 3mA and 1mA, respectively.  $Rox=2\mu m$ .

The number of transverse modes is proportional to the oxide aperture, referred to Eq.(3-21). Figure 4.2 demonstrates the single lasing mode which is LP01,  $V=2.1748$ ; The single mode is suit for high speed operation. Figure 4.3 demonstrates the multimode behavior of VCSELs that represents 7 modes. The LP02 and LP41 are dominated when it reached steady state. The multimode emission is preferred for some applications, such as multimode fiber communication.

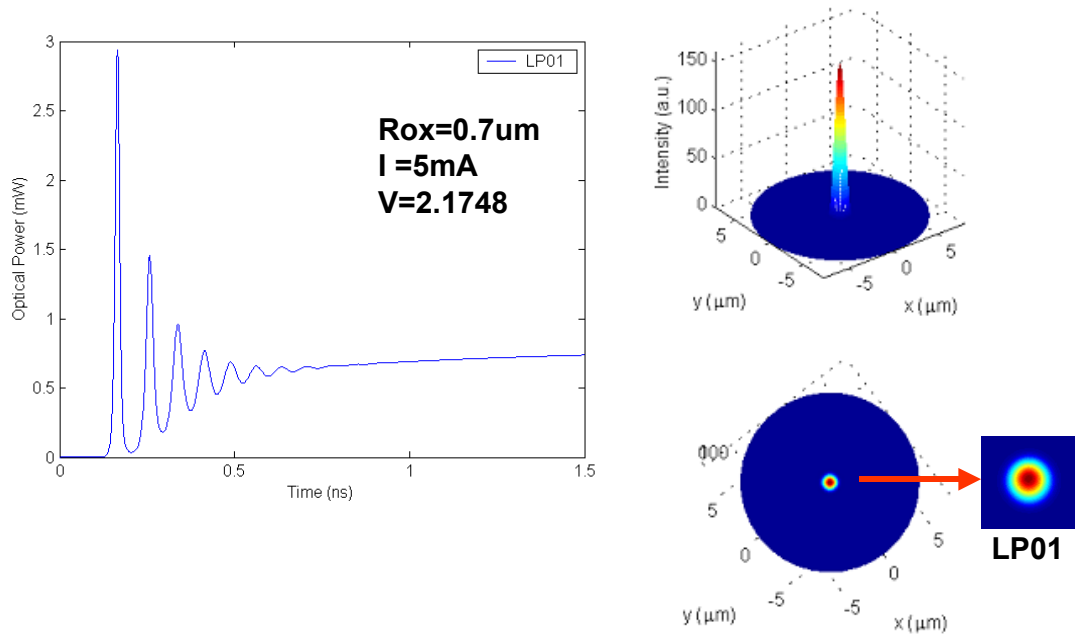


**Figure 4.2** The single mode operation. The LP01 mode is called fundamental mode.

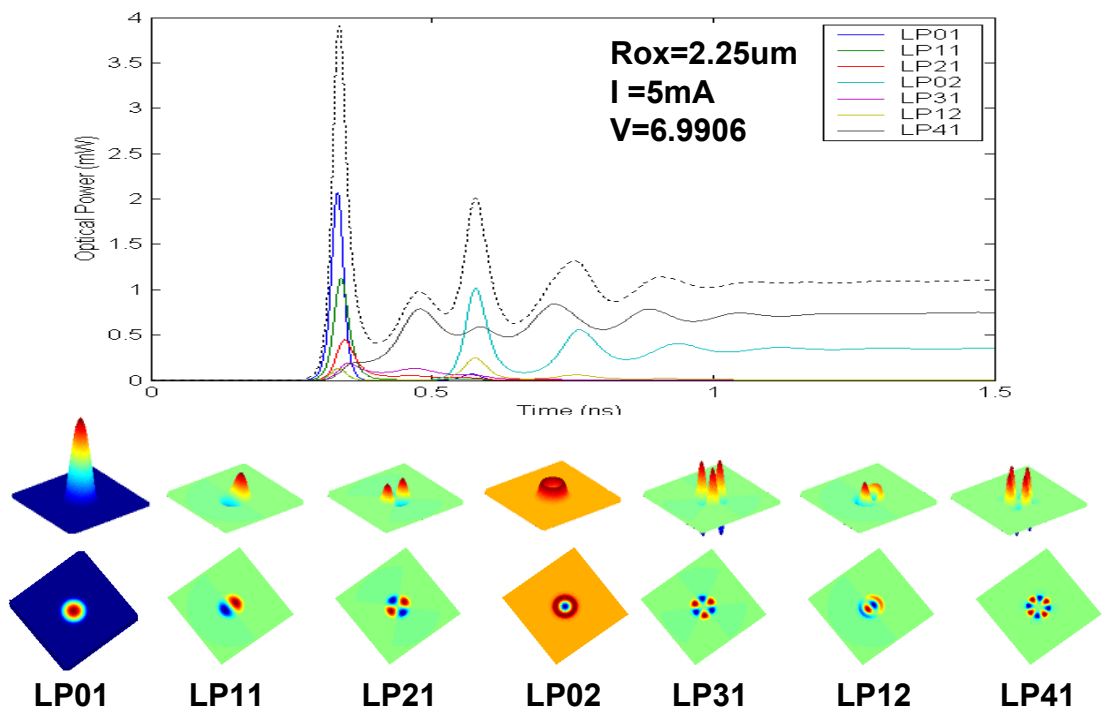


**Figure 4.3** The multimode behavior of VCSELs. The output optical profile are also shown. (dash line: total power)

The mode competition can be represented by the transient response due to the time evolution of nonuniformly carrier distribution, is given in Figure 4.4 and 4.5. The carrier distribution is strongly related to the current confinement in the active region and can be evaluated by current spreading effect, referred to section-3 in this chapter. In order to simplify this investigation for easy comparison, the oxide aperture radius is set to 1um to limit only two modes can propagate and azimuthal carrier distribution is not taken into account. In Figure 4.4-(a), the LP11 mode dominates over the entire duration after the first 0.65ns. The mode switching is caused by the severe carrier hole burning in the core region, that leading a suppression of fundamental mode LP01 and a higher order mode is emphasized. It is noted that the change of carrier distribution enhances the coupling efficiency of LP11 mode over the fundamental mode LP01 is shown in Figure 4.4-(b). That provides the evidence of current is not well confined in the core and a spatial hole burning of the carrier density occurs during the first overshoot of fundamental mode due to the stimulated recombination.

In contrast, Figure 4.5 shows the transient response with current confinement consideration. The corresponding time evolution of carrier distribution is shown in Figure 4.5-(b). It can be seen that the current confinement structure suppresses the higher order mode during the turn-on transient response of the device. The carrier distribution exhibits less hole burning throughout the transient period and the coupling efficiency between the carrier distribution and optical field profile of LP11 mode maintains at a low value. It also produces higher output power than the structure without current confinement. The above results show that the dynamic behavior of transient modes exhibit different characteristics of device. Figure 4.6 shows the time evolution of optical intensity. Figure 4.6-(a) shows much optical intensity variation in the duration of mode switching.

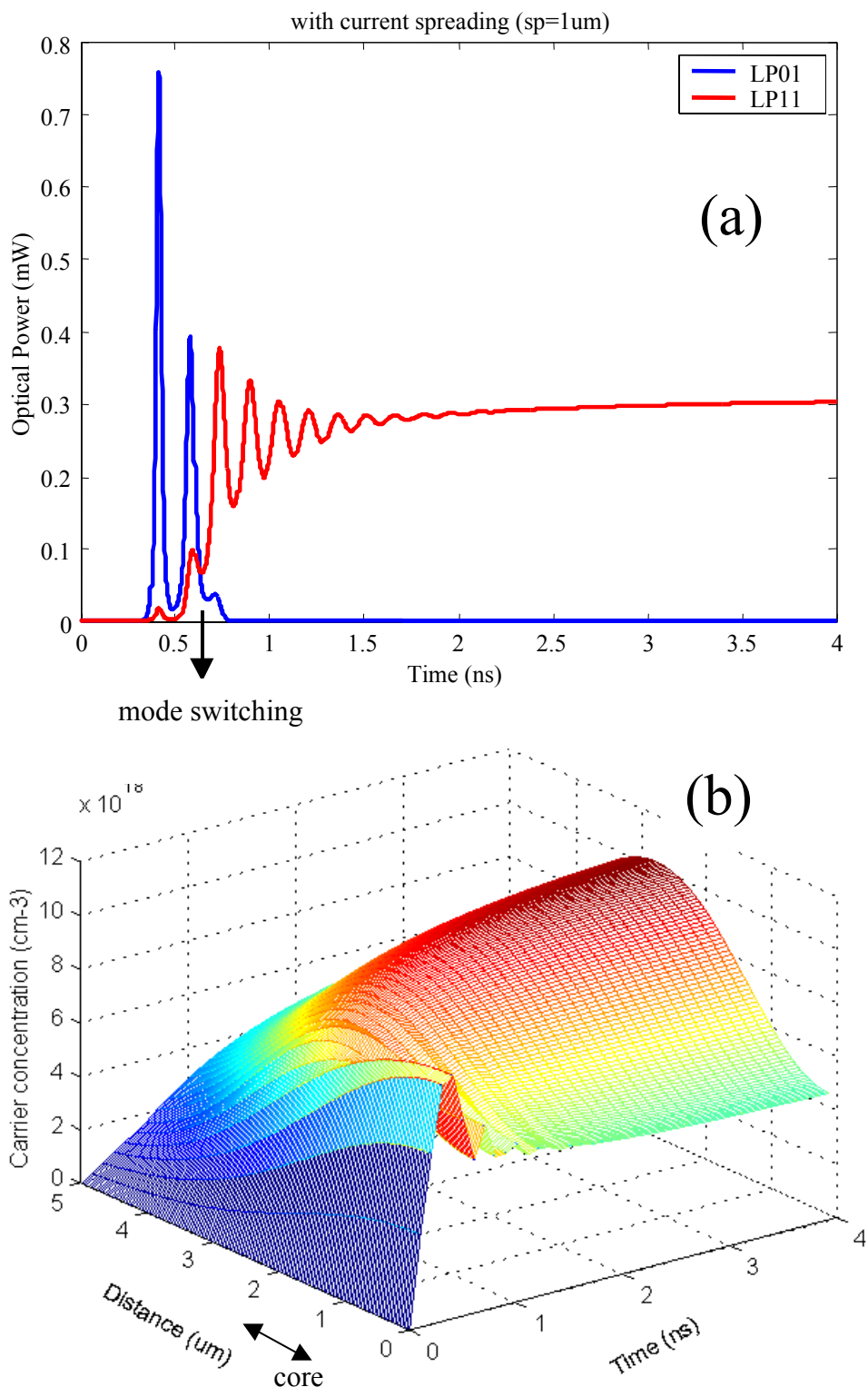


**Figure 4.4** Without current confinement (sp=1um), for (a) The transient response of two transverse modes. (b) The corresponding time evolution of carrier distribution.  $\text{Rox}=1\mu\text{m}$ ,  $I=2\text{mA}$ ,  $\text{DN}=15\text{cm}^2/\text{s}$ .

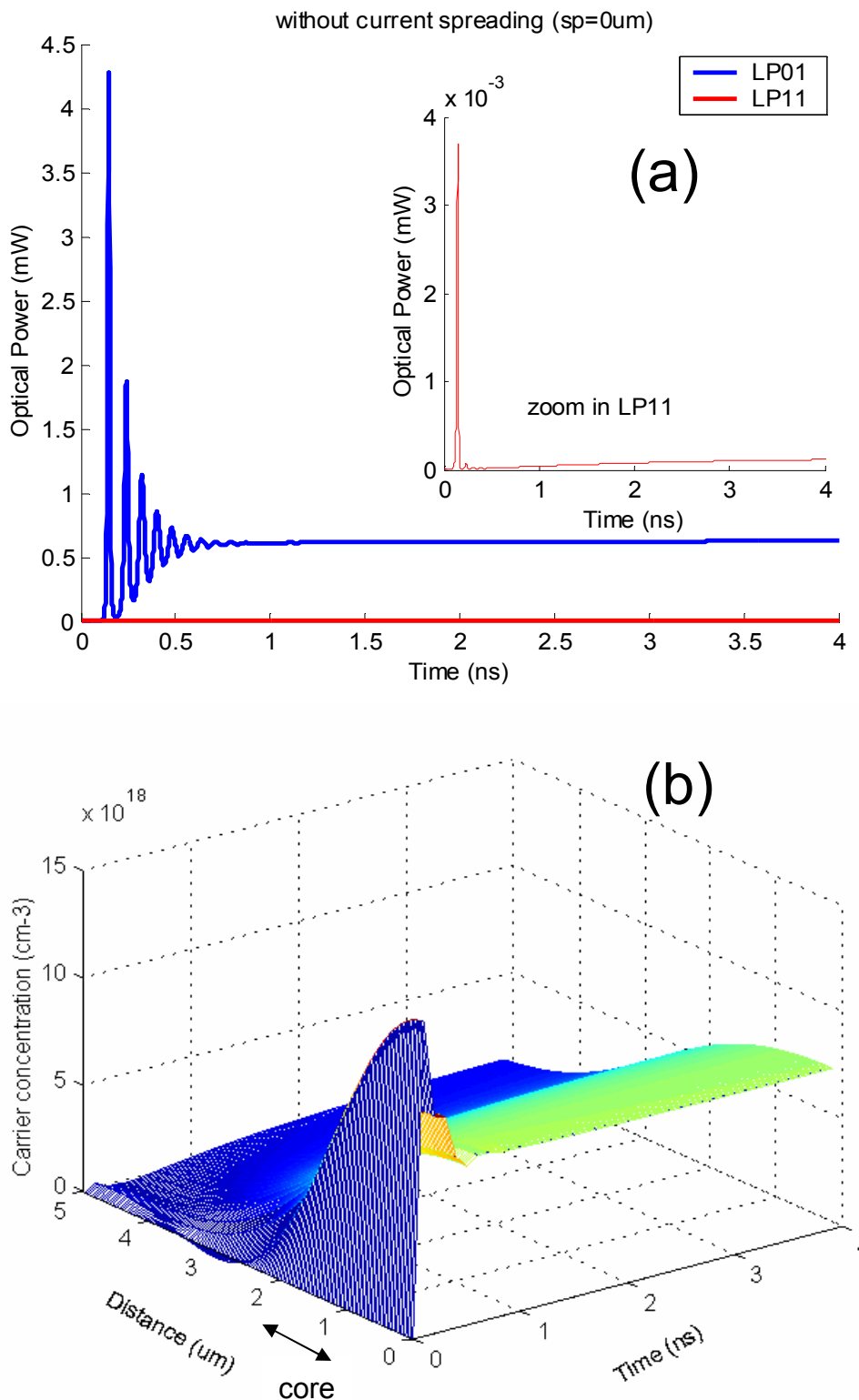


**Figure 4.5** With current confinement ( $sp=0\mu\text{m}$ ), for (a) The transient response of two transverse modes. (b) The corresponding time evolution of carrier distribution.  $R_{ox}=1\mu\text{m}$ ,  $I=2\text{mA}$ ,  $DN=15\text{cm}^2/\text{s}$ .

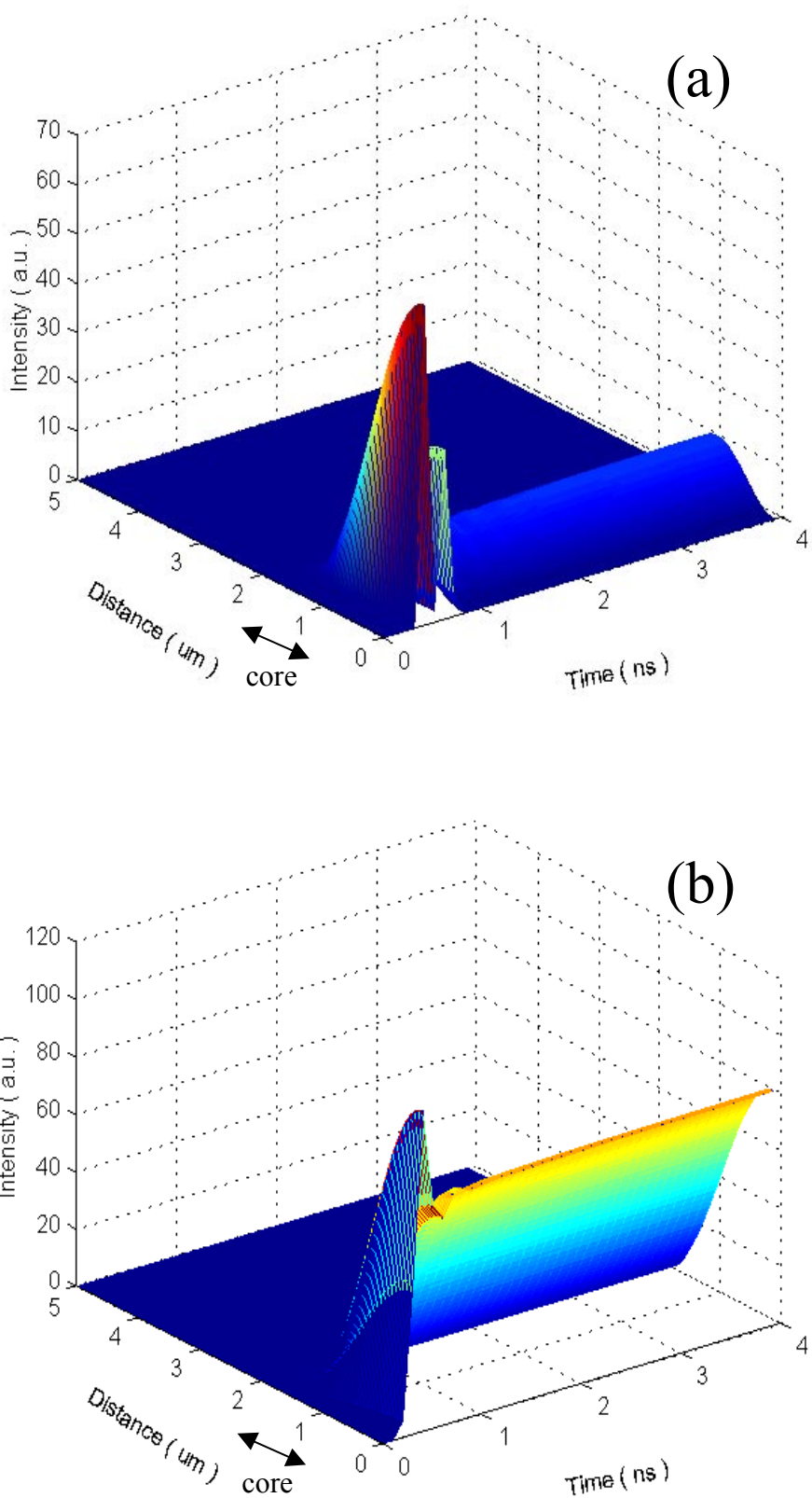


**Figure 4.6** The time evolution of optical intensity, for (a) Without current confinement ( $sp=1\mu m$ ) (b) With current confinement ( $sp=0\mu m$ ).  $R_{ox}=1\mu m$ ,  $I=2mA$ ,  $DN=15cm^2/s$ .

## 4.2 L-I curve

The relation between optical output power and the injected current provides the most fundamental information on the operation of semiconductor lasers or light emitting diodes. The L-I curve is the most important characteristics of lasers. The threshold current and quantum efficiency can be determined by it. To design a high performance VCSEL, the main issue is the tradeoff between low threshold current and high quantum efficiency. Low threshold primarily implies high mirror reflectivity, fewer quantum wells, and smaller device size. High quantum efficiency primarily implies lower mirror reflectivity, more quantum wells, and reduced optical losses. Assuming the ideal case in which the L-I curve is linear above threshold current, is given in Figure 4.7 that shows the L-I curve of size-dependent excluding thermal effect. The small size shows lower threshold current and slope efficiency. The current required to achieve a given output power  $P_{out}$  is simply related to both threshold current  $I_{th}$  and external quantum efficiency  $\eta_{ext}$ , is given as:

$$I = I_{th} + \frac{q}{h\nu} \frac{P_{out}}{\eta_{ext}} \quad (4-1)$$

where  $q$  is electron charge,  $h\nu$  is photon energy [7].

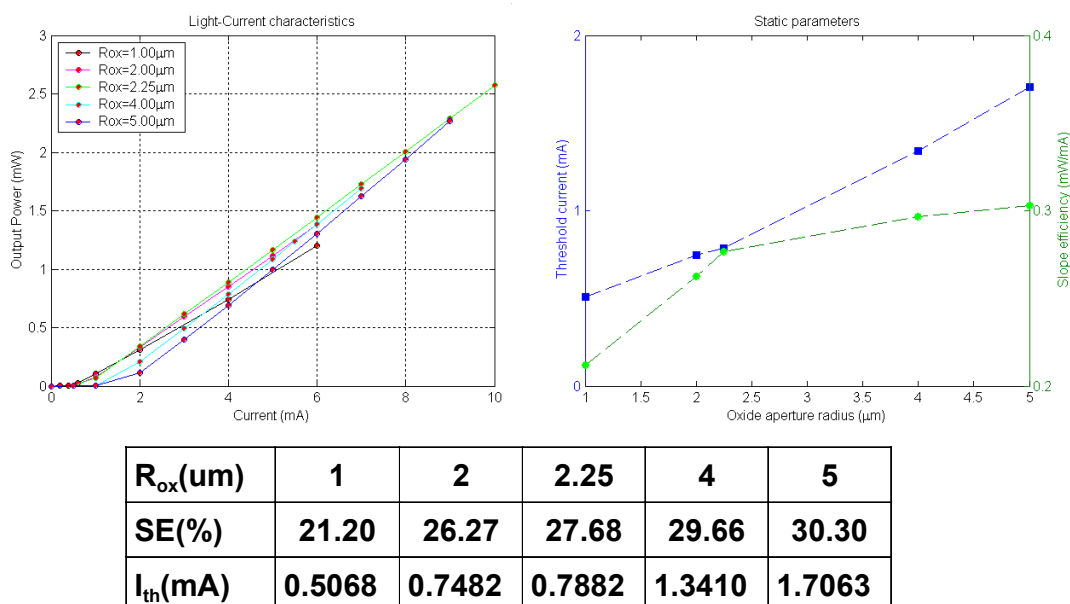


**Figure 4.7** L-I curve : the thermal effect is neglected.

In a practical models which thermal effect must be taken into account. It is found that the characteristics of L-I curve is determined by its cavity loss and thermal resistance  $R_{th}$ , which are size dependent. The value of  $R_{th}$  used in the thermal model is extracted from the experimental data and it presents the thermal effects of VCSELs with  $C_{th}$  parameter [6]. Figure 4.8 illustrates the smaller size represents the smaller slope efficiency and threshold current. The other observation is the happening of output power roll over is earlier in smaller size than larger size. The small size shows higher temperature-sensitivity than large one.

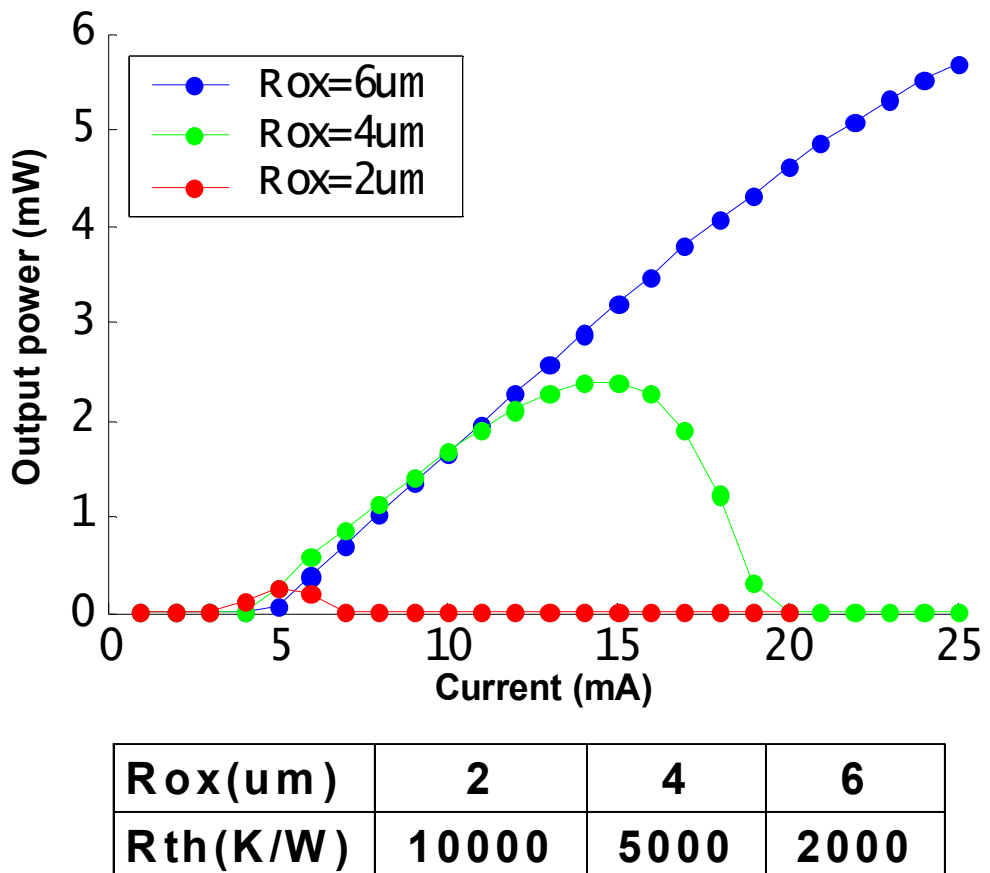


**Figure 4.8** L-I curve and its size-dependent parameters: the thermal effect is included.

## 4.3 Spatial Hole Burning

The performance of VCSELs could be degraded due to the poor overlap between the optical and carrier distribution results in the phenomenon of spatial hole burning (SHB). To understand the formulation of spatial hole burning (SHB), it can rely on the visualized capability of MATLAB as shown in Figure 4.9. The left-side accounts for the radial carrier distribution (1D) while right-side accounts for the radial and azimuthal carrier distribution (2D).

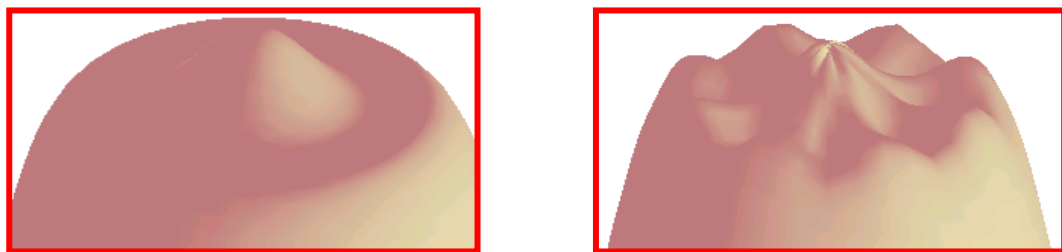


**Figure 4.9** The carrier concentration distribution represents the phenomenon of SHB for 1D(left) and 2D(right).

Figure 4.10 shows the profile of SHB inside the active region. It is noted that the higher injected current, the greater SHB. In the “hole” region, it implies this region with a high photon density, the locally higher stimulated recombination will deplete the carriers. In order to maintain the threshold gain necessary for lasing, the carrier density will increase in the adjacent regions with lower photon intensity, creating a hole in the carrier distribution. This hole will reduce the lateral carrier confinement for the main optical mode and increase the overlap between the carrier and side-modes, leading to a mode-jump or multimode operation. Since the depth of the hole also varies during modulation, it will affect the dynamic response of the VCSELs.

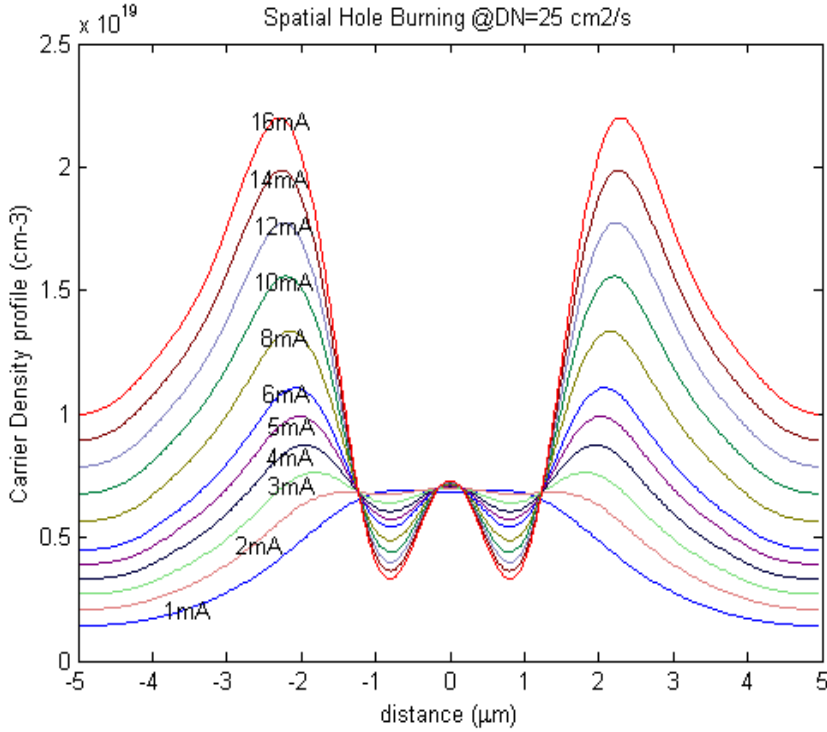


**Figure 4.10** The carrier concentration in various bias currents.  $R_{ox}=2.25\mu\text{m}$ .

The influence of SHB on the dynamic properties of VCSELs can be investigated by the carrier diffusion constant and injected current spreading. Figure 4.11-(a)(b) represents the carrier distribution in the active region with different diffusion constant-DN and current spreading coefficient-sp conditions. The left-set of Figure 4.11 is ideal case ( $sp=0$ ) while right-set is more realistic ( $sp=1\mu\text{m}$ ). In this figure, it represents the spreading coefficient is dominated in the core region while diffusion constant is dominated in the cladding region. It is clear from Figure 4.11-(a)(b) that a higher DN results in the larger effective diffusion length and leads to more carriers flow out of active region, therefore, the higher threshold current is expected even it shows less SHB.

For circular-ring contact or circular-disc contact, the azimuthal injection profile is usually set to 1(i.e., it is uniform in azimuthal coordinate), therefore only the radial injection profile is considered. A expression to describe the radial current spreading is given [10],

$$\begin{aligned} \frac{J(r,t)}{J_0(t)} &= 1, & r \leq R_{ox} \\ &= \exp\left(\frac{R_{ox} - r}{sp}\right), & r \geq R_{ox} \end{aligned} \quad (4-1)$$

where  $J_0$  is current density at the edge ( $R_{ox} = r$ ),  $sp$  is effective diffusion length of the injection carrier,  $R_{ox}$  is oxide aperture radius.

Two parameters are investigated to analyze how does the SHB to affect the dynamic response of VCSELs. One is diffusion constant-DN and the other is current spreading coefficient-sp. The transient response is shown in Figure 4.11-(c)(d). Comparing the damping oscillation and the output power of (c) and (d) of Figure 4.11, the (c) shows higher oscillation rate and power than (d) in the same injected current. It implies the (c) with lower DN might have higher resonance frequency and suit for high-speed operation than (d) if the current spreading can be reduced [3]. However, this derivation can be proven in [1].

$$\gamma \propto f_r^2 \quad (4-2)$$

where  $\gamma$  is damping factor,  $f_r$  is resonance frequency.

Figure 4.11-(c)(d) also points out the higher DN results in longer time for device start to lase and exhibits higher threshold current. In the previous work of S.F.Yu who proposed the higher DN results in higher resonance frequency and better modulation performance if the carrier transport effect is considered, and set both output power are equal in steady-state [11].

The lateral diffusion of QW carriers only slightly dampens the relaxation peak, but doesn't significantly affect the modulation bandwidth is given in Figure 4.11-(e) which the current spreading effect is eliminated, therefore, it is suit for the studying of modulation response in diffusion constant-dependent [12]. A realistic analysis is shown in Figure 4.11-(f), it represents slightly shift in the bandwidth and a low-frequency roll-off is also observed. The carriers in different regions will exhibit quite different dynamic responses due to the variation in the mode intensity. In the right-set of Figure 4.11, the larger DN results in the lightly SHB effect, but the amount of carriers in the cladding region is comparable with core region. It implies that the carriers are not well confined in the core where is active region, hence, the less power is produced. The severe carrier concentration in the cladding region will degrade the intrinsic modulation operation, therefore, the overall modulation response is limited [13].

In Figure 4.11-(f), the small DN leads to the enhancement of ROF (relaxation-oscillation frequency) can also be explained by the severe SHB due to the short carrier diffusion length inside the active layer that shows better carrier confinement, therefore, the ROF is enhanced even the obvious SHB. On the other hand, high-order modes may be excited by SHB at high output power. This is the tradeoff

between the high modulation bandwidth and single-mode operation, but the single-mode operation of VCSELs can be maintained by using tapered optical waveguide or diffused quantum-well structure without reduction of SHB [11].

The conclusion of above, the SHB is affected by diffusion constant and current spreading, but the modulation response is dominated by current spreading rather than diffusion constant. The bandwidth reduction, oscillation frequency overdamped and the low frequency roll-off are caused by the severe current spreading is shown in Figure 4.12.

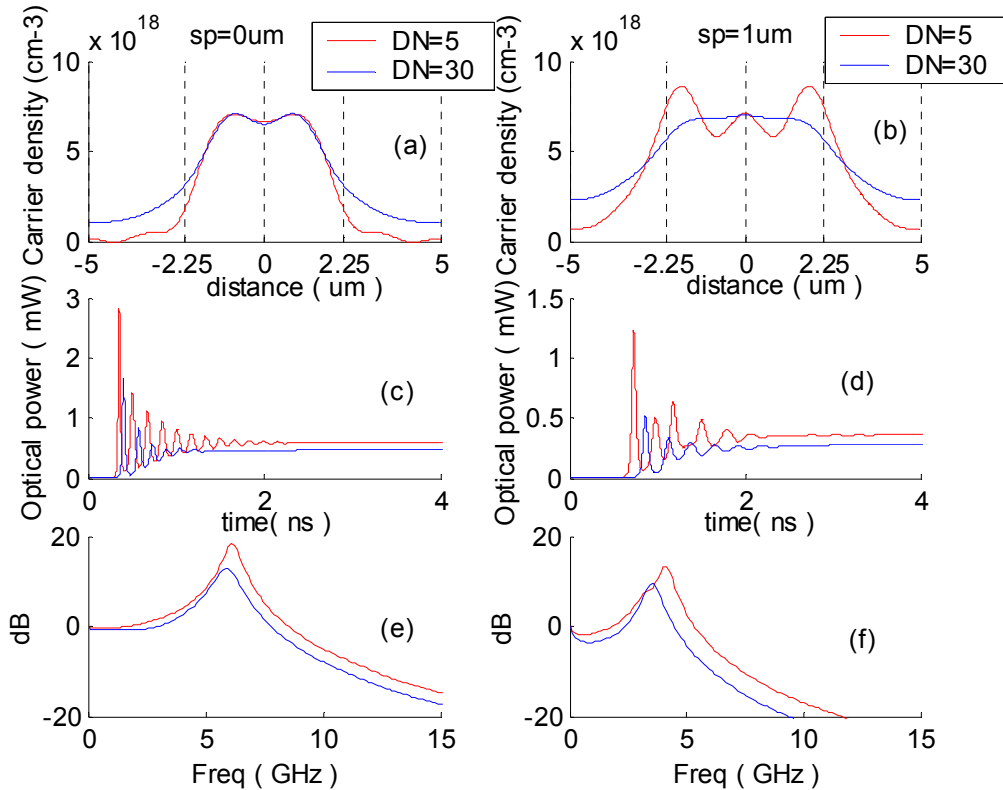


**Figure 4.11** The influence of SHB on the dynamic responses of VCSELs, the time and frequency domain are included. The  $sp=0\text{um}$  for left-set, and  $sp=1\text{um}$  for right-set. For (a)(b) the influence of diffusion constant and current spreading coefficient on SHB, (c)(d) transient response, (e)(f) modulation response.  $R_{ox}=2.25\text{um}$ ,  $I=2\text{mA}$ .

It is noted that for high injection current case, for example 10mA, the high DN shows higher resonance frequency. This is because for high injection current the carrier refill capability is more expected than the carrier confinement, which is expected in lower injection current.

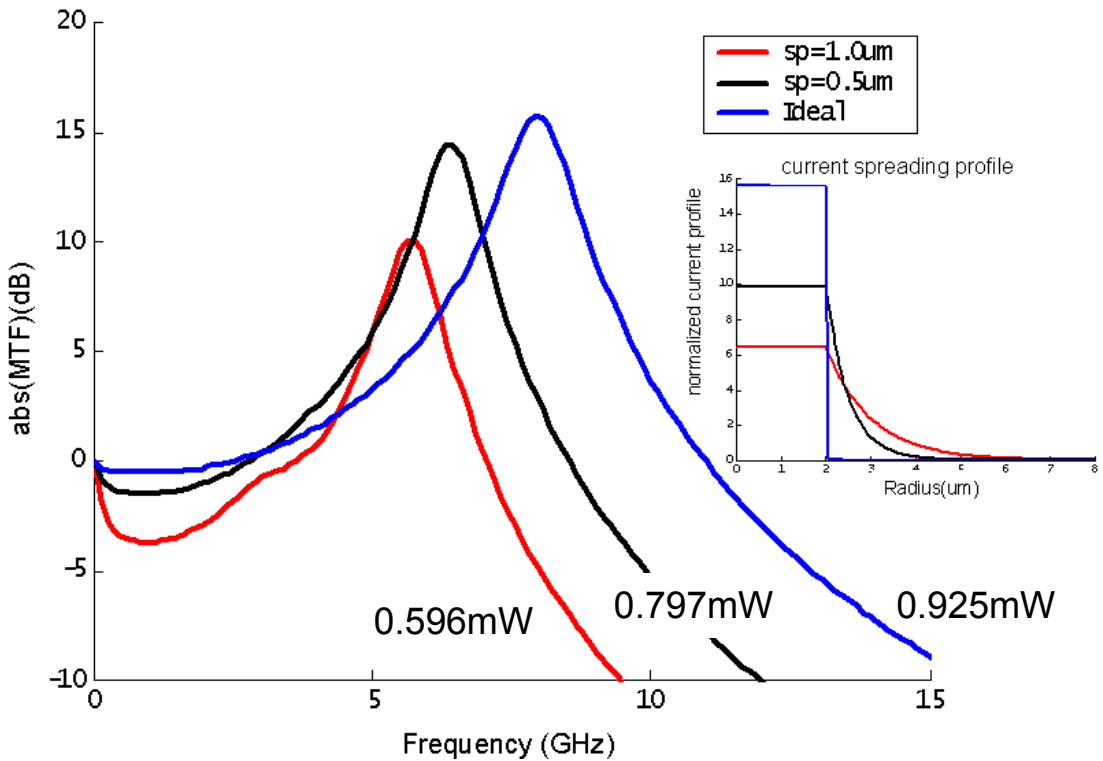


**Figure 4.12** The influence of current spreading coefficient on the current injection profile and modulation properties.  $R_{ox}=2\mu m$ ,  $I=3mA$ ,  $DN=15cm^2/s$ .

## 4.4 Thermal effect

The VCSELs represent its sensitivity to the thermal effect due to its extremely small cavity volume. There are two major effects related to the temperature increased in the cavity, one is the mismatch between the peak of gain spectrum and lasing peak, the other one is the leakage current. The leakage current is the carrier leakage out of the quantum wells that is related to the temperature-dependency of the bandgap and quasi-Fermi level [7]. Cavity temperature is calculated as a function of the difference between electrical and optical power. Figure 4.13 illustrates the influence of thermal effects on the dynamic response of VCSELs. It is noted that the higher leakage current results in severe differential gain reduction due to the more temperature increased in the cavity. Furthermore, the reduction of differential gain can also result in a dramatic limitation of the high frequency capability of the laser. The laser is shown to briefly reach approximately 3.5mW after turn-on for bias current equals to 15mA. The temperature then increases slowly, and the optical power is reduced to its

steady-state value, close to 2.5mW.

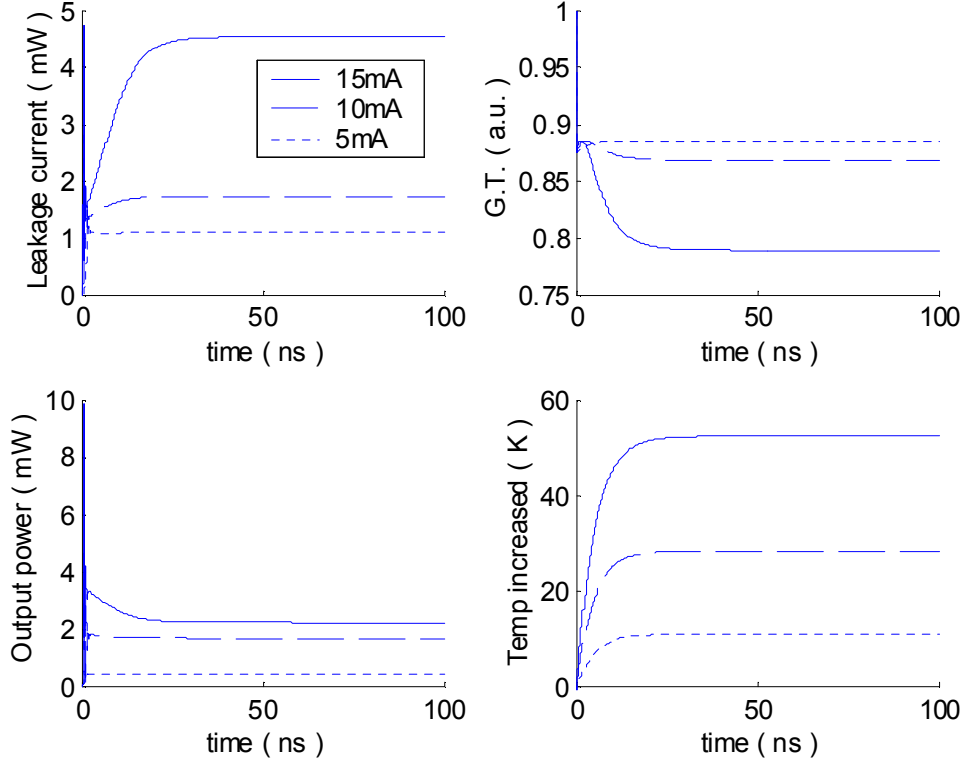


**Figure 4.13** The thermal effect of current-dependent.  $R_{ox}=4\mu m$ ,  $R_{th}=5000K/W$ .

## 4.5 Small Signal Modulation

Figure 4.14 represents the modulation response of VCSELs. The higher bias current shows wider bandwidth. It is noted that the increasing current results in the losses increased and high level injection. Figure 4.15 depicts the aperture dependence of resonance frequency. It indicates that reducing the oxide aperture will decrease threshold current that results in the ROF increased. They can be explained by the expressions

$$fr \propto \sqrt{\frac{g_0}{V_a} (I - I_{th})} \quad (4-3)$$

where  $g_0$  is differential gain,  $I$  is bias current,  $I_{th}$  is threshold current,  $V_a$  is active volume [14].

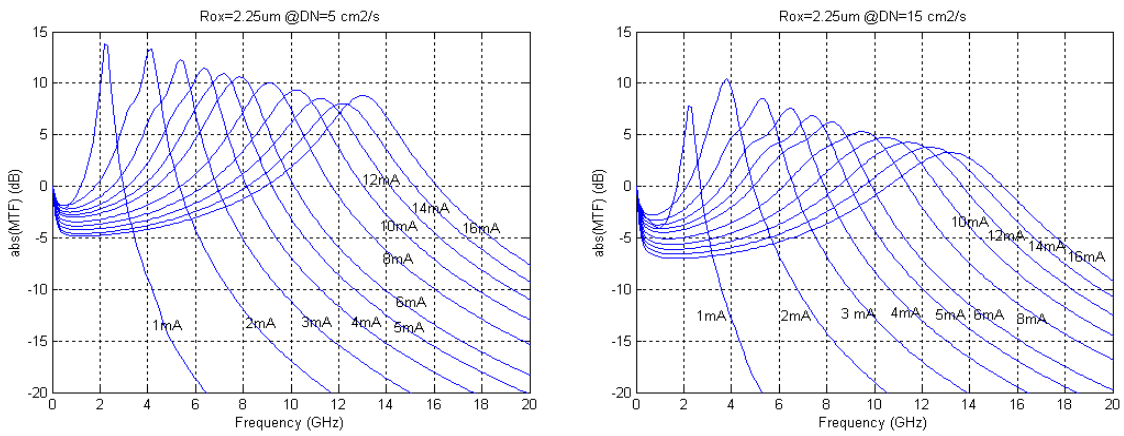


**Figure 4.14** The small signal modulation with different bias current without thermal effect.

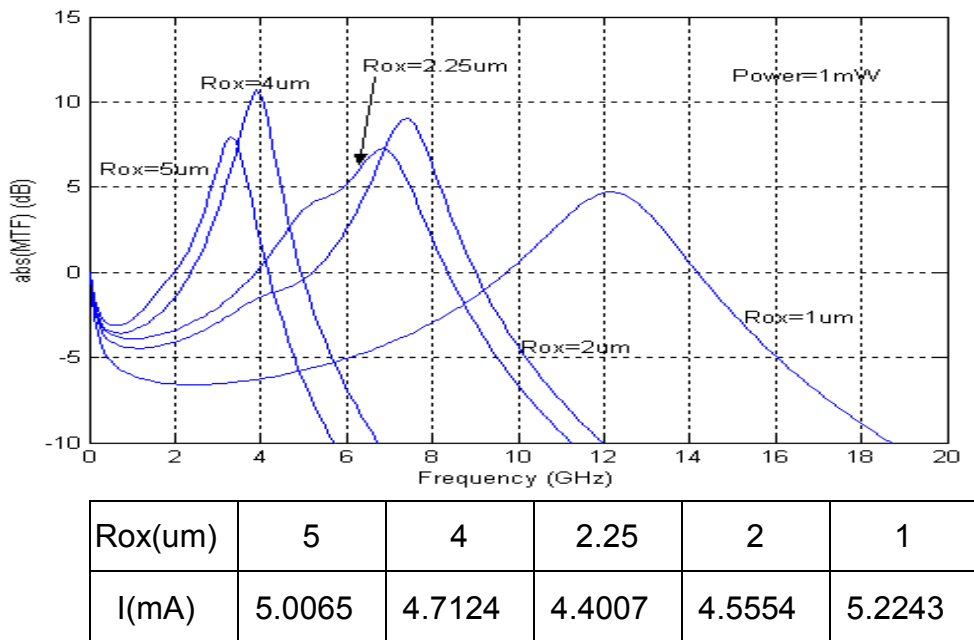


**Figure 4.15** The small signal modulation with different size. The output power is 1mW.

The other important factor to indicate the performance of VCSELs is D factor is shown in Figure 4.16. Higher D factor is always desired. The high value of the D factor for the single-mode VCSEL is a result of the small cavity and gain volumes, the single transverse mode, and the corresponding high photon density [15]. As a figure

of merit, the modulation current efficiency factor (MCEF) is often given to specify the increase of the 3dB corner frequency of the abs(MTF) as

$$MCEF \equiv \frac{f_{3dB}}{\sqrt{I - I_{th}}} \quad (4-4)$$

and the D-factor is given as

$$D - \text{factor} \equiv \frac{f_r}{\sqrt{I - I_{th}}} \quad (4-5)$$

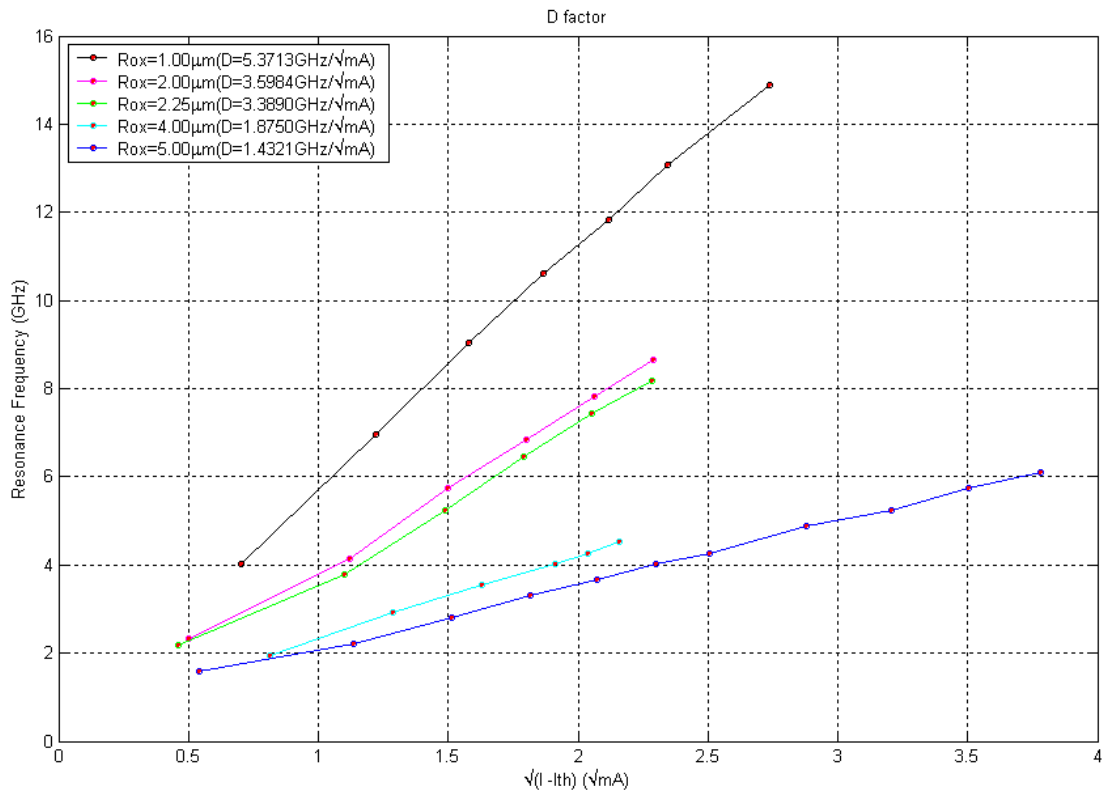


**Figure 4.16** D factor

# CHAPTER 5

## CONCLUSIONS

This paper describes the theoretical modeling technique to investigate the electrical and optical characteristics of VCSELs. First, the application of VCSELs and capability of models are introduced in chapter 1. Next, the derivation of rate equations and modeling can be found in chapter 2, 3. Chapter 4 represents the simulation results and numerical analysis via MATLAB.

The models are based on the formulation of rate equations and associate with thermal effect, carrier diffusion effect, current spreading effect, spatial hole burning (SHB). Those effects are the crucial parameters to dominate the performance of VCSELs. The output transverse optical profile can be approximated to LP modes due to the weakly index-guided structure. The calculation of LP-modes is based on the electromagnetic theory, and its solution can be represented in the Bessel function through a series of mathematical transformation.

The thermal effect introduces the optical gain suppressed and leakage current increased that result in the rollover of the L-I curve. The VCSELs with small oxide aperture represents the highly sensitive to temperature generated inside the laser cavity due to its high thermal resistance exhibits low thermal conductivity behavior. The influence of SHB on the characteristics of VCSELs can be investigated by the carrier diffusion and injected current spreading. The current spreading was found to be more dominative over carrier diffusion on the dynamic response while the carrier transport is neglected. A higher bandwidth and better low frequency response are obtained under low current spreading condition that results in low threshold current. Also, in the lower injection current condition the resonance frequency slightly increased by the smaller carrier diffusion under the same current spreading condition even the severe SHB was seen. The severe SHB shows the excitation of high-order mode, so that the mode competition is evidence. This is the tradeoff between the high modulation bandwidth and single-mode operation. On the opposite, in the higher current condition, the high carrier diffusion shows higher bandwidth due to its better carrier refill capability.

In order to construct an accurate and high efficient simulation models, it relies on three parts : 1) the understanding of laser theory that would provide the knowledge to generate a models in theory-based, and the understanding of the interaction of various phenomena is also necessary to reach a consistent results. 2) using mathematical technique to translate the theory-based models into math-based models that would much improve the computation time. 3) the programming skills and simulation platform are turning the theory to practical application, a flexible programming algorithm is always desired.

# REFERENCES

1. Marc Xavier Jungo, " Spatiotemporal VCSEL Model for Advanced Simulations of Optical Links," Hartung-Gorre Verlag Konstanz, 2003.
2. A. Valle, J. Sarma, and K. A. Shore, "Spatial Holeburning Effects on the Dynamics of Vertical Cavity Surface-Emitting Laser Diodes," IEEE J. Quantum Electronics, vol 31, no.8, pp.1423-1431, Aug.1995.
3. BAHAA E. A. SALEH, MALVIN CARL TEICH, " Fundamentals of Photonics," John Wiley & Sons, Inc., 1991.
4. Siu Fung Yu, " Analysis and design of vertical cavity surface emitting lasers," John Wiley & Sons, Inc., 2003.
5. Govind P. Agrawal, Niloy K. Dutta, "Semiconductor lasers," 2nd edition, AT & T, 1993.
6. E. D. Kyriakis-Bitzaros and G. Halkias, "Thermal Resistance Evaluation of High-Speed VCSELs: An Isothermal Optical Transient Technique," IEEE Photonics Tech. Lett. vol 14, no.3, pp.269-271, Mar.2002.
7. Jeff W.Scott, Randall S. Geels, Scott W. Corzine and Larry A. Coldren, "Modeling Temperature Effects and Spatial Hole Burning to Optimize Vertical-Cavity Surface-Emitting Laser Performance," IEEE J.Quantum Electron., vol 29, no.5, pp.1295-1308, May.1993.
8. JOHN A. BUCK, " Fundamentals of OPTICAL FIBERS," John Wiley & Sons, Inc., 1995.
9. Ajoy Ghatak, K. Thyagarajan, " Introduction to fiber optics," Cambridge University Press, 1998.
10. N. K. Dutta, "Analysis of current spreading, carrier diffusion, and transverse mode guiding in surface emitting lasers," J. Appl. Phys. vol.68, pp.1961-1963,1990.
11. S. F. Yu, "Dynamic behavior of vertical-cavity surface-emitting lasers," IEEE J. Quantum Electron., vol.32, no.7, pp.1168–1179, 1996.

12. S. F. Yu, W. N. Wong, P. Shum, and E. H. Li, "Theoretical analysis of modulation response and second-order harmonic distortion in vertical-cavity surface-emitting lasers," *IEEE J. Quantum Electron.*, vol.32, pp.2139–2147, 1996.
13. Yang Liu, Wei-Choon Ng, Benjamin Klein, and Karl Hess, "Effects of the Spatial Nonuniformity of Optical Transverse Modes on the Modulation Response of Vertical-Cavity Surface-Emitting Lasers," *IEEE J. Quantum Electron.*, vol.39, no.1, pp.99–108, Jan. 2003.
14. O. Kjebon, R. Schatz, S. Lourdudoss, S. Nilsson, and B. St\_alnacke, "Modulation response measurements and evaluation of MQW InGaAsP lasers of various designs," *SPIE Proc.*, vol.2684, pp.138-152, 1996.
15. Christina Carlsson, Hans Martinsson, Richard Schatz, John Halonen, and Anders Larsson, "Analog Modulation Properties of Oxide Confined VCSELs at Microwave Frequencies," *JOURNAL OF LIGHTWAVE TECHNOLOGY*, vol.20, no.9, Sep.2002.

# 作者簡介

## 個人資訊

- 姓名：羅俊麟
- 性別：男
- 生日：1971



## 工作經驗

1997/7 至今

美商瓦里安(股)公司台灣分公司(新竹市)

◆ 客戶服務工程師,資深客戶服務工程師,主任工程師

- 熟悉半導體設備”離子植入機”的製程原理,設備操作,保養與維修
- 滿足客戶需求,解決客戶問題,並維持與客戶的良好關係
- 公司內部人員培訓
- 編製公司的專業訓練教材
- 負責之客戶
  - 6 吋 晶圓廠：UMC-6A, MXIC-I, ATC, Winbond-II.
  - 8 吋 晶圓廠：UMC-8A, UMC-8B, UMC-8C, UMC-8E, UMC-8F, SiS, MXIC-II, tsmc-8AB
  - 12 吋 晶圓廠：ProMos-300mm.

## 教育程度

2002/9 – 2004/6 國立交通大學(新竹市) 電機資訊學院電子與光電學程碩士班畢業

1991/9 – 1995/6 國立臺灣科技大學(台北市) 電子工程系畢業

1987/9 – 1990/6 高雄市立高級工業職業學校(高雄市) 電子工程科畢業

## 榮譽事蹟

- 曾至美國 Boston 接受離子植入機的專業訓練三次(1997,1999,2001)
- 榮獲聯電集團/USIC 之最佳廠商獎(1999)
- 榮獲聯電集團/8C 之最佳廠商獎(2002/2)
- 榮獲聯電集團/8F 之最佳廠商獎(2002/5)
- 榮獲國立交通大學/電機資訊學院碩士在職專班/電子與光電組之書卷獎(2004/3)